



# Structure of the Full-Length Bacteriophytochrome from the Plant Pathogen *Xanthomonas campestris* Provides Clues to its Long-Range Signaling Mechanism

Lisandro Horacio Otero<sup>1,2</sup>, Sebastián Klinke<sup>1,2</sup>, Jimena Rinaldi<sup>1</sup>, Francisco Velázquez-Escobar<sup>3</sup>, María Andrea Mroginski<sup>3</sup>, María Fernández López<sup>3</sup>, Florencia Malamud<sup>4</sup>, Adrián Alberto Vojnov<sup>5</sup>, Peter Hildebrandt<sup>3</sup>, Fernando Alberto Goldbaum<sup>1,2</sup> and Hernán Ruy Bonomi<sup>1</sup>

**1 - Fundación Instituto Leloir—IIBBA-CONICET**, Av. Patricias Argentinas 435 (C1405BWE), Buenos Aires, Argentina

**2 - Plataforma Argentina de Biología Estructural y Metabólica PLABEM**, Av. Patricias Argentinas 435 (C1405BWE), Buenos Aires, Argentina

**3 - Institut für Chemie**, Technische Universität Berlin, Sekr. PC 14, Straße des 17. Juni 135 (10623), Berlin, Germany

**4 - UNSAM Campus Miguelete IIB—Instituto de Investigaciones Biotecnológicas**, Av. 25 de Mayo y Francia (B1650KNA), Buenos Aires, Argentina

**5 - Instituto de Ciencia y Tecnología Dr. Cesar Milstein**, Fundación Pablo Cassará, CONICET, Saladillo 2468 (C1440FFX), Buenos Aires, Argentina

**Correspondence to Hernán Ruy Bonomi:** [hbonomi@leloir.org.ar](mailto:hbonomi@leloir.org.ar)

<http://dx.doi.org/10.1016/j.jmb.2016.04.012>

Edited by M. Guss

## Abstract

Phytochromes constitute a major superfamily of light-sensing proteins that are reversibly photoconverted between a red-absorbing (Pr) and a far-red-absorbing (Pfr) state. Bacteriophytochromes (BphPs) are found among photosynthetic and non-photosynthetic bacteria, including pathogens. To date, several BphPs have been biophysically characterized. However, it is still not fully understood how structural changes are propagated from the photosensory module to the output module during the signal transduction event. Most phytochromes share a common architecture consisting of an N-terminal photosensor that includes the PAS2–GAF–PHY domain triad and a C-terminal variable output module. Here we present the crystal structure of the full-length BphP from the plant pathogen *Xanthomonas campestris* pv. *campestris* (*XccBphP*) bearing its photosensor and its complete output module, a PAS9 domain. In the crystals, the protein was found to be in the Pr state, whereas diffraction data together with resonance Raman spectroscopic and theoretical results indicate a ZZZssa and a ZZEssa chromophore configuration corresponding to a mixture of Pr and Meta-R state, the precursor of Pfr. The *XccBphP* quaternary assembly reveals a head-to-head dimer in which the output module contributes to the helical dimer interface. The photosensor, which is shown to be a bathy-like BphP, is influenced in its dark reactions by the output module. Our structural analyses suggest that the photoconversion between the Pr and Pfr states in the full-length *XccBphP* may involve changes in the relative positioning of the output module. This work contributes to understand the light-induced structural changes propagated from the photosensor to the output modules in phytochrome signaling.

© 2016 Elsevier Ltd. All rights reserved.

## Introduction

Sunlight delivers vital radiant energy to our planet but it also provides spatial and temporal information sensed by organisms across all kingdoms. Biological photoreceptors detect light by sensing wavelength and intensity, transducing this information into

cellular signaling pathways. For a long time, there had been no evidence for photoreceptors being functional in non-photosynthetic prokaryotes. However, over the last decade, several studies have shown that these proteins play many important roles including a role in bacterial infectious processes [1–3].

Phytochromes are photosensors that can transduce light by a reversible photoconversion between two typical defined states: (i) red-absorbing (Pr) and (ii) far-red-absorbing (Pfr). These photoreceptors constitute a major family first described in plants, but also present in algae, fungi, cyanobacteria and other bacteria [4,5]. Prototypical phytochromes exhibit a Pr ground state and a dark conversion from Pfr to Pr. On the other side, the bathy-type phytochromes show a Pfr ground state and a Pr-to-Pfr dark conversion [6]. Most phytochromes share a common architecture consisting of an N-terminal photosensory module and a C-terminal variable output module. The photosensor detects the light signal, whereas the output module is responsible for transducing this information into a biological effect by means of a specific activity. The photosensor is composed of three consecutive domains: (i) Period/ARNT/Single-minded (PAS2), (ii) cGMP phosphodiesterase/adenylate cyclase/FhlA transcriptional activator (GAF), and (iii) phytochrome specific (PHY) [4]. Output modules are often composed of a single histidine kinase (HK) module; however, further variants include (i) an HK–response regulator pair, (ii) c-di-GMP cyclase/phosphodiesterase, or (iii) PAS domains, among others [7,8].

The photochemical properties of phytochromes reside in its open-chain tetrapyrrole (bilin), a bound chromophore that is buried within the GAF domain and that typically forms a covalent bond between the C3<sup>2</sup> atom of the side chain of ring A and a conserved cysteine residue of the phytochrome. The photochemistry takes place around the double bond between the bilin rings C and D, where an E to Z and Z to E isomerization of the C15 = C16 methine bridge rotates the D pyrrole ring defining the Pr (ZZZssa) and Pfr (ZZEssa) states, respectively [7]. The precise nature of the bilin differs within the phytochrome subfamilies: plant phytochromes incorporate phytychromobilin, cyanobacterial phytochromes phycocyanobilin, and bacteriophytochromes (BphPs) and fungal phytochromes biliverdin IX $\alpha$  (BV). All apo-phytochromes that are able to covalently bind the corresponding bilin perform this action autocatalytically by means of the bilin-lyase activity from the GAF domain [7].

To date, only few BphPs have been associated with specific biological responses [9,10]. *Xanthomonas campestris* pv. *campestris* (*Xcc*), a non-photosynthetic phytopathogenic bacterium that infects cruciferous plants, encodes a single BphP protein (*XccBphP*) that regulates its virulence<sup>†</sup>. Several BphP structures have been determined; however, none of them include a complete output module in addition to the photosensory module. Consequently, the structural determinants involved in photoreception and signaling between the photosensory and the output module remain elusive owing to the lack of a complete structural model. Here we provide novel

data to address this issue by means of the full-length *XccBphP* crystal structure combined with spectroscopic, computational, and biochemical data.

## Results

### *XccBphP* is a bathy-like BphP

Sequence analysis on *XccBphP* revealed a conserved PAS2–GAF–PHY domain triad (Fig. 1) and a C-terminal PAS9 domain, according to a Pfam classification [11]. The PAS2–GAF–PHY triad represents the typical photosensory module from group-I canonical phytochromes found in bacteria, plants and fungi, whereas the PAS9 domain is the output module for this protein [4]. As the *XccBphP* PAS9 domain has no predicted enzymatic activity, it is likely to mediate protein–protein interactions in the signaling pathway [12]. Noteworthy, group-I phytochromes that contain a PAS domain immediately adjacent to the photosensor (alone or in combination with other domains) represent 48% of the Pfam database sequences to date. As expected, size exclusion chromatography (SEC) and zinc-induced fluorescence experiments [13] showed that BV binds both to the recombinant full-length *XccBphP* [14]—hereafter referred to as only *XccBphP*—and to a construct harboring the photosensory module alone ( $\Delta$ PAS9) (Fig. S1).

Far-red irradiation (733 nm) leads to the photoconversion of both *XccBphP* and  $\Delta$ PAS9 holoproteins into a pure Pr species, as indicated by the lack of the Pfr absorption band at 752 nm (Fig. 2a). Irradiation with red (630 nm) promotes the formation of the Pfr form, with a Pfr:Pr ratio of ~2:1 (Fig. 2b). In the absence of actinic light, dark conversion leads to the accumulation of the Pfr state, albeit to a different extent in the full-length protein and the truncated version (Fig. 2a). The  $\Delta$ PAS9 construct exhibits a typical bathy-type BphP behavior, for which Pfr is the thermodynamically stable state, since a pure Pfr state is obtained after 21 h in the dark (Fig. 2b). In contrast to other representatives of the bathy phytochrome group [6], the presence of the PAS9 domain in *XccBphP* modulates the final Pfr:Pr ratio to ~6:1 (Fig. 2b), indicating thermal equilibrium between Pfr and Pr. We therefore denote *XccBphP* as a bathy-like phytochrome. The thermal Pfr/Pr equilibrium can be explained by the different quaternary arrangements in  $\Delta$ PAS9 (monomer) and *XccBphP* (dimer, see Fig. 7), which might influence the chromophore binding pocket environment, and consequently the dark reversion thermodynamics [15].

To monitor the assembly process by UV–Vis absorption spectroscopy, both apoproteins were incubated in the dark with BV. *XccBphP* and  $\Delta$ PAS9 assembled in less than 5 min as pure Pr forms. After 21 h in the dark, Pfr was the prevailing form in both

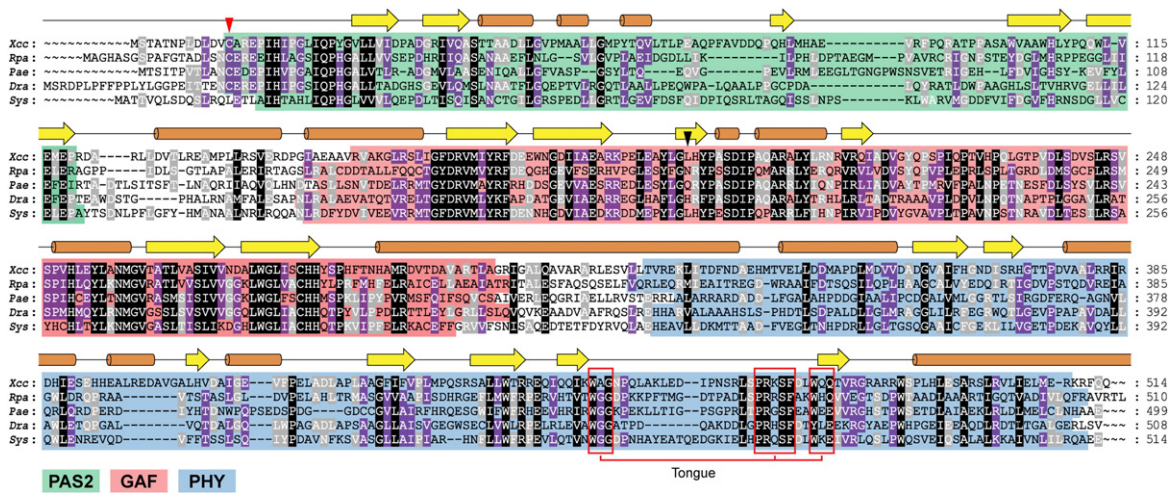


**Fig. 1.** Sequence alignment from BphP photosensory modules with known three-dimensional structures. *Xanthomonas campestris* (A0A0H2XCS3, *Xcc*), *Rhodospseudomonas palustris* (B3Q7C0, *Rpa*), *Pseudomonas aeruginosa* (Q9HWR3, *Psa*), *Deinococcus radiodurans* (Q9RZA4, *Dra*), and *Synechocystis* sp. (Q55168, *Sys*) PAS2 (green), GAF (red), and PHY (blue) domain sequences obtained from the Pfam server and aligned using ClustalO. Black, violet and gray backgrounds represents 100%, 80%, and 60% conservation within similarity groups, respectively. The schemed secondary structures are derived from the model obtained from the *XccBphP* crystal structure (this work).  $\alpha$ -Helices and  $\beta$ -sheets are depicted as orange barrels and yellow arrows, respectively. The conserved N-terminal cysteine residues in BphPs are indicated with a red arrow, corresponding to Cys13 in *XccBphP*. Gln188 from *P. aeruginosa* (which aligns to Leu193 in *XccBphP*) is indicated with a black arrow. The conserved “tongue” motif is highlighted in red boxes.

cases (Fig. 2c), in analogy to the dark adaptation of the holoproteins (Fig. 2a). For a kinetic analysis of the dark adaptation, *XccBphP* and  $\Delta$ PAS9 were first illuminated with far-red light for 10 min to generate the Pr state. The subsequent dark processes were monitored by UV–Vis absorption spectroscopy for 21 h. *XccBphP* exhibits a long half-time for the dark conversion ( $t_{1/2} = 7.49$  h), corresponding to rate constants of  $\sim 4.3 \cdot 10^{-5}$  and  $0.72 \cdot 10^{-5} \text{ s}^{-1}$  for the Pr  $\rightarrow$  Pfr and Pfr  $\rightarrow$  Pr dark reaction, respectively. In the absence of the PAS9 domain, the dark conversion to Pfr is accelerated almost by a factor of 10 (Fig. 2d), pointing to the modulation of the dark reversion of the chromophore by the output module as observed recently for the bathy phytochrome Agp2 from *Agrobacterium tumefaciens* [16]. Fig. 2e summarizes the photoinduced and thermal equilibrium states from *XccBphP*.

### Full-length holo-*XccBphP* exhibits conserved structural features from other BphPs

In this work, we solved the crystal structure of the full-length *XccBphP* holoprotein at 3.25 Å resolution (Fig. 3a and b). The structure comprises the photosensory module as well as a complete output module. Crystallization and crystal handling was carried out minimizing light exposure (see details in Materials and Methods). The final refined model shows two chains in the asymmetric unit (A and B) with favorable stereochemistry, and values for  $R_{\text{work}}$  and  $R_{\text{free}}$  of 20.5% and 25.5%, respectively (Table 1).

Both monomers are essentially equivalent, with a  $C^{\alpha}$ -r.m.s.d. value of 1.72 Å for 566 aligned residues. The electron density maps are continuous in both chains, except for the initial 11 N-terminal residues, the loop comprising residues 456–472 in both monomers (which corresponds to the tongue region projection, see description below), and the residue ranges 124–126, 570–572, and 603–604 in monomer A.

Each monomer consists of four lobes clearly defined by the classical PAS2–GAF–PHY domain triad and a PAS9 domain. The long linker helices that serve as connectors within the GAF–PHY and PHY–PAS9 domain pairs (Fig. 3b and c) are the principal elements of the typical “helical spine,” where the dimer interface is assembled.

Like other group-I phytochromes, *XccBphP* includes the typical figure-of-eight knot [17] that crosses over residues between the PAS2 and GAF domains enclosing the chromophore interaction pocket (Fig. 3d). Here, residues 17–29 from the N-terminal PAS2 domain cross through the loop formed by residues 216–247 from the GAF domain. This knot is mainly stabilized by a small two-stranded antiparallel  $\beta$ -sheet moiety formed by the residues Leu23–Ile24 (PAS2) and Ser224–Pro225 (GAF). Moreover, the conserved Ile24 residue lies within a hydrophobic pocket formed by the side chains from the residues Leu30, Ile226, Val238, Leu240, Val243, and Leu245. The highly conserved “tongue” or “hairpin” (W(G/A)G, PRxSF, and (W/Y/F)x(E/Q) motifs) (Fig. 1) corresponds to a protrusion from

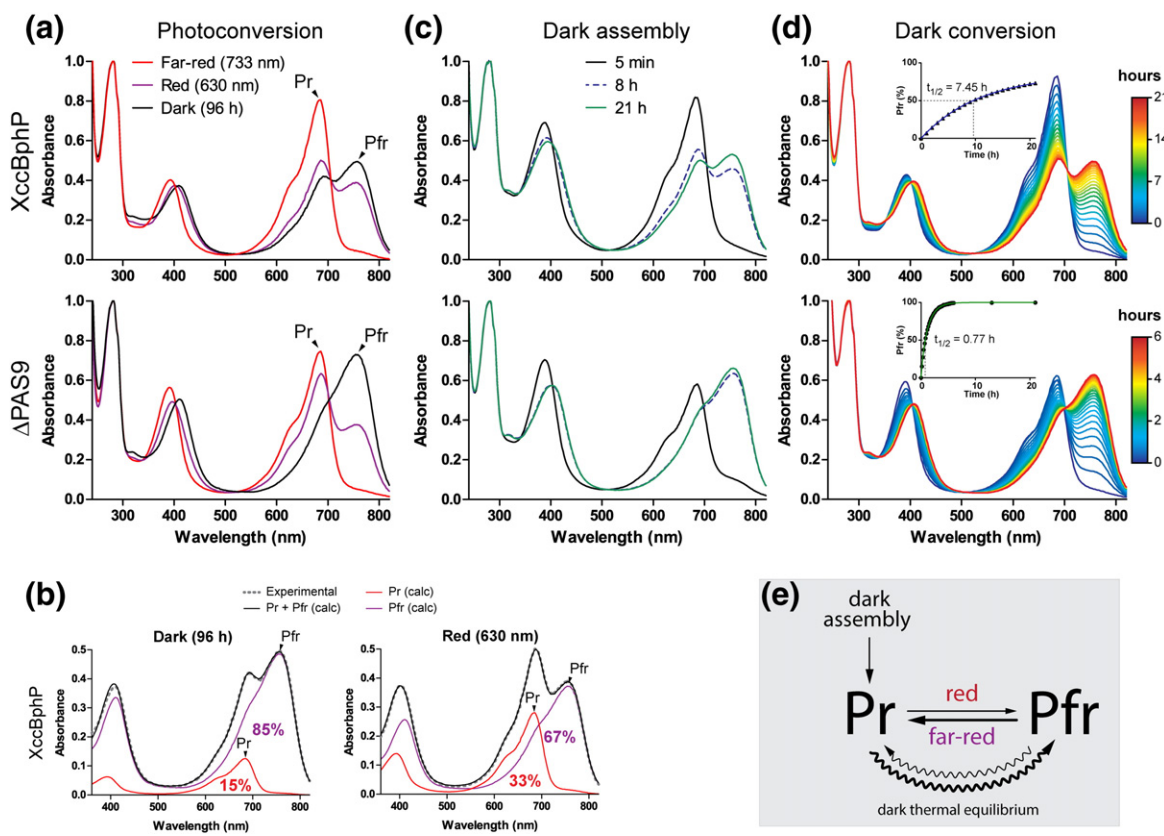


**Fig. 2.** UV/Vis spectral properties of the XccBphP and its photosensory module. (a) Absorption spectra of dark-adapted XccBphP and  $\Delta$ PAS9 after illumination with red or far-red light. The contributions from the red (Pr) and far-red (Pfr) absorbing states are indicated. (b) XccBphP Pr and Pfr contributions calculated from the UV-Vis absorption spectra in panel (a). Experimental data from dark-adapted or red illuminated XccBphP (dashed gray curves) and Pr + Pfr calculations (black curves) using Eq. (1). Pr and Pfr contributions were calculated from Eqs. (2) and (3). (c) XccBphP and  $\Delta$ PAS9 apoproteins absorption spectra measured at different times after addition of BV. All experiments were performed in the dark. (d) Dark reversion kinetics from XccBphP and  $\Delta$ PAS9. Holoproteins were irradiated with far-red light and then kept in the dark. Absorption spectra were recorded for a period of 21 h. Insets: Pr-to-Pfr dark kinetic plots. Pfr proportions were calculated according to Eq. (6). Estimated half-times ( $t_{1/2}$ ) are indicated. (e) The XccBphP photocycle corresponds to a bathy-like phytochrome exhibiting a dark assembly in the Pr state and displaying dark conversion toward a Pfr/Pr equilibrium enriched in the Pfr form. Far-red light converts XccBphP completely into the Pr form, while red illumination partially converts it into Pfr.

the PHY domain (residues 446–483) that serves as a gatekeeper to the chromophore binding pocket [18]. The tongue shows a two-stranded antiparallel  $\beta$ -sheet conformation characteristic of the Pr state (Fig. 3b and Table 2). Altogether, the photosensor of XccBphP exhibits a very similar secondary structure and overall fold compared to those of other structurally characterized group-I BphPs, as judged by r.m.s.d. values below 3 Å (Table S2).

In both monomers, BV is covalently bound to Cys13 in the PAS2 domain *via* a thioether bond formed with the vinyl side chain of ring A (bond length 1.86 and 2.05 Å for chains A and B, respectively). The chromophore pocket (Fig. 4a), enclosed by a  $\beta$ -sheet and three  $\alpha$ -helices, comprises 23 highly conserved residues in the phytochrome family [4,19]. Here, Asp199 from the DIP (Asp-Ile-Pro) motif interacts through its side chain

with the oxygen atom from ring A, and *via* its backbone carbonyl oxygen atom with the nitrogen atoms from rings A and B. Indeed, this residue is stabilized by a conserved salt-bridge interaction with Arg472 from the tongue region. On the opposite side, His252 and His282 close the pocket (Fig. 4a). This “sandwiched” chromophore pocket formed by the latter residues is widely conserved in phytochrome structures [8,19]. Both residues are crucial for stabilizing the protonated chromophore structure in the photochemical Pr-to-Pfr conversion. The ring B propionate is in an extended conformation as a consequence of its salt-bridge interactions with Arg214 and Arg246 (Fig. 4a), whereas the ring C propionate is missing in the electron density map, indicating a high mobility (Fig. 4b). Different BphPs may vary in their propionate interactions according to the signaling transmission route to the corresponding

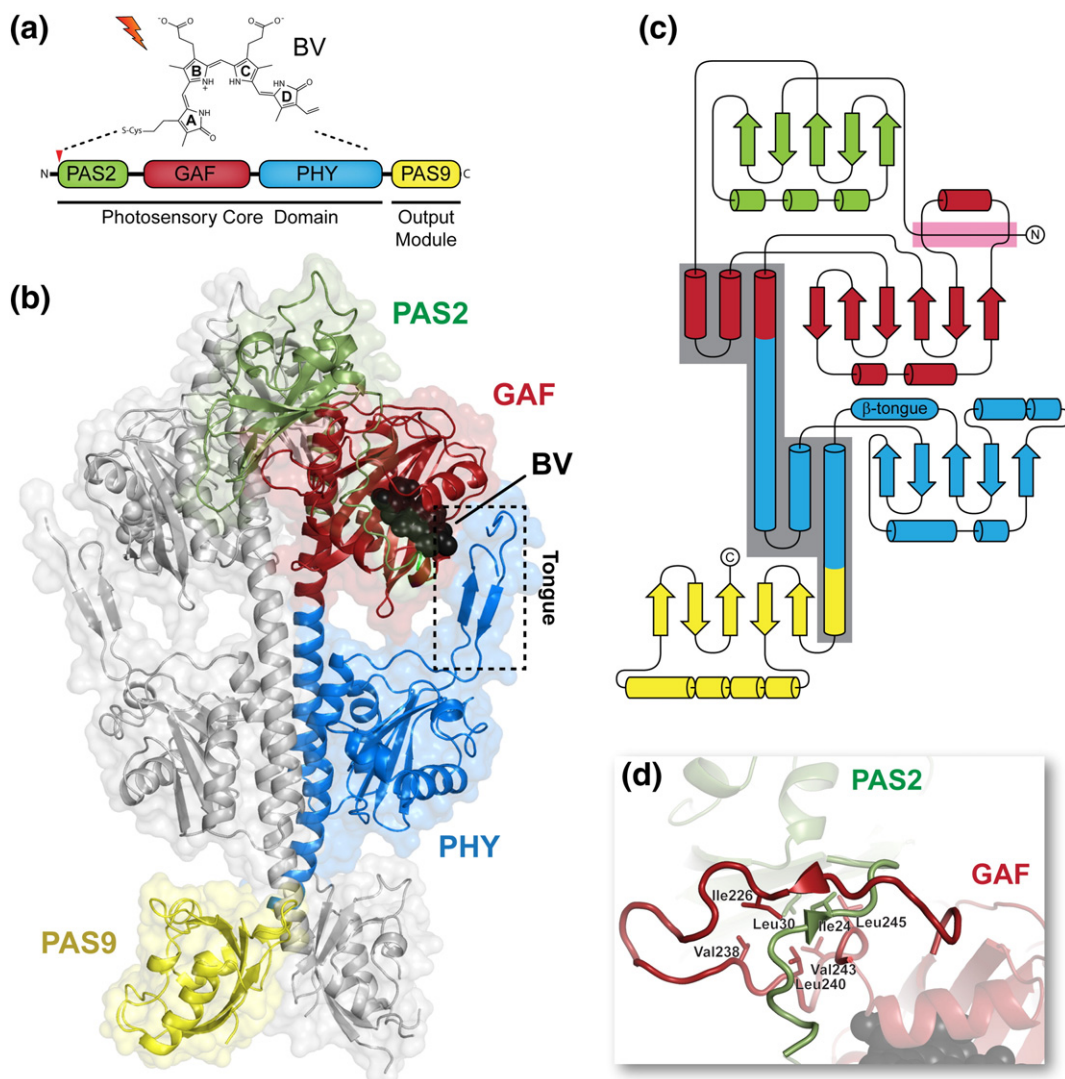


**Fig. 3.** Crystal structure of full-length *XccBphP*. (a) Domain architecture of *XccBphP*. The PAS2 (green), GAF (red), PHY (blue), and PAS9 (yellow) domains are depicted; the same color code is applied to all figures in this work. The photosensory module binds to the chromophore BV from a conserved cysteine residue indicated by a red arrow (Cys13). (b) Ribbon representation of *XccBphP* bound to BV (black spheres). The tongue region is highlighted in a dashed box. The solvent-accessible surface calculated by PyMOL is shown in the background. (c) The *XccBphP* topologic diagram. The  $\beta$ -strand tongue region is indicated and the helical spine is shadowed in gray and the location of the figure-of-eight knot is highlighted in pink. (d) Detailed view of the figure-of-eight knot from the *XccBphP* in the Pr state. Ribbon representation of the knot structure that crosses over residues between the PAS2 and GAF domains. BV is shown as spheres. The knotted interface is highlighted with darker colors. The hydrophobic core within the knot and the relevant residues participating are shown in the inset.

effector domains [20]. A conserved pyrrole water molecule is found to be coordinated by the NH groups of the pyrrole rings A, B, and C, and the residues Asp199 and His252. This set of interactions might be critical for the correct proton transfer that takes place during photoconversion [21,22]. On the other side of the chromophore, Tyr168 and Tyr195, which are essential for photochemistry and signaling [19,23], are located within the ring D pocket (Fig. 4c).

### The crystal structure shows heterogeneous chromophore configuration

The rings A, B, and C are well-fitted into the density map (Fig. 4b). A pairwise structural comparison of the GAF domain with other BphPs in Pr (*DrBphP* and *Cph1*) [18,24] or Pfr states (*PaBphP* and *RpBphP1*) [25,26] reveals a similar domain scaffold in which the positions of the *XccBphP* BV

**Table 1.** Data collection and refinement statistics for XccBphP

Statistics	
PDB code	5AKP
Data collection	
Synchrotron source	SOLEIL
Beamline	PROXIMA 1
Number of frames	600
Oscillation step (deg)	0.2
Detector distance (mm)	577.75
Wavelength (Å)	0.97857
Exposure per frame (s)	0.2
Indexing and scaling	
Cell parameters	$a$ (Å) 103.94 $b$ (Å) 103.94 $c$ (Å) 344.57 $\alpha = \beta = \gamma$ (deg) 90
Space group	$P4_32_12$
Resolution limit (Å)	3.25
No. of total reflections	216820
No. of unique reflections	30865
Average multiplicity <sup>a</sup>	7.0 (7.5)
$\langle I/\sigma(I) \rangle$	19.6 (2.4)
$R_{meas}$	0.116 (1.488)
$R_{pim}$	0.042 (0.516)
Completeness (%)	99.9 (100.0)
No. of chains per asymmetric unit	2
Solvent content (%)	62
Overall $B$ -factor (Wilson plot, Å <sup>2</sup> )	94
Refinement	
Resolution range (Å)	41.75–3.25
No. of protein atoms	9390
No. of ligand atoms	103
No. of water molecules	2
$R$	0.205
$R_{free}$	0.255
Rms deviations from ideal values [74]	
Bond lengths (Å)	0.010
Bond angles (deg)	1.2
Average $B$ -factor (Å <sup>2</sup> )	
Protein	114
Ligand	129
MolProbity validation [59]	
Clashscore	11.61
MolProbity score	3.03
Ramachandran plot	
Favored (%)	90.4
Allowed (%)	6.8
Disallowed (%)	2.8

<sup>a</sup> Values in parentheses correspond to the highest resolution shell (3.43–3.25 Å).

rings *A*, *B*, *C*, and ring *B* propionate somewhat mimic the Pr configuration (Fig. 4d). However, no clear electron density was found in the area where the ring *D* is placed (Fig. 4b), so neither a ZZZssa (Pr) nor a ZZEssa (Pfr) chromophore configuration could be unambiguously established solely on the crystallographic data. To address this issue, we carried out resonance Raman (RR) experiments on three XccBphP crystals similar to those used for the X-ray structural analysis (Fig. 5a, middle) [16,27]. All crystal spectra show the same prominent band at 1626 cm<sup>-1</sup>. This band could be readily assigned to

**Table 2.** Comparison among non-redundant BphP structures reported in the PDB bearing a complete photosensory module

Name	Organism	PDB code	Resolution (Å)	Type	Condition	Protein			Chromophore			
						Tongue	Tyr1/Tyr2	Helical spine	State	Bilin	Configuration	State
PaBphP	<i>Pseudomonas aeruginosa</i>	3C2W	2.90	Bathy	Dark	$\alpha$	Opened/Closed	Straight	Pfr	BV	ZZEssa	Pfr
PaBphP	<i>Pseudomonas aeruginosa</i>	3NOP	2.80	Bathy	Light induced	$\alpha$	Opened/Closed	Straight	Pr-like	BV	ZZZssa-like (L1)	Pr-like
PaBphP	<i>Pseudomonas aeruginosa</i>	3NOT	2.70	Bathy	Light induced	$\alpha$	Opened/Closed	Straight	Pr-like	BV	ZZZssa-like (L2)	Pr-like
PaBphP	<i>Pseudomonas aeruginosa</i>	3NOU	3.00	Bathy	Light induced	$\alpha$	Opened/Closed	Straight	Pr-like	BV	ZZZssa-like (L3)	Pr-like
RpBphP1	<i>Rhodospseudomonas palustris</i>	4GW9	2.90	Bathy	Dark	$\alpha$	Opened/Closed	Straight	Pfr	BV	ZZEssa	Pfr
RpBphP2	<i>Rhodospseudomonas palustris</i>	4S21	3.25	Canonical	Dark	$\beta$	Closed/Opened	Bent	Pr	BV	ZZZssa	Pr
RpBphP3	<i>Rhodospseudomonas palustris</i>	4R70	2.85	Canonical*	Dark	$\beta$	Closed/Opened	Bent	Pr	BV	ZZZssa	Pr
DfBphP	<i>Deinococcus radiodurans</i>	4O01	3.24	Canonical	Light	$\alpha$	Closed/Opened	Straight	Pr/Pfr	LBV	ZZZssa/ZZEssa	Pr/Pfr
DfBphP	<i>Deinococcus radiodurans</i>	4O0P	3.80	Canonical	Dark	$\beta$	Closed/Opened	Bent	Pr	LBV	ZZZssa	Pr
Cph1	<i>Synechocystis</i> sp.	2VEA	2.21	Canonical	Dark	$\beta$	Closed/Opened	Bent	Pr	CYC	ZZZssa	Pr
XccBphP	<i>Xanthomonas campestris</i>	5AKP	3.25	Bathy-like	Dark	$\beta$	Closed/Opened	Bent	Pr	BV	ZZZssa/ZZEssa	Pr/Meta-R

Tyr1/Tyr2 corresponds to conserved Tyr168/Tyr195 in XccBphP and its respective counterparts in other BphP structures.

BV, biliverdin; LBV, 2(R),3(E)-phytychromobilin; CYC, phycoerythrobilin.

\* *RpBphP3* adopts the Pr state ( $\lambda_{max} \sim 700$  nm) in the dark, but upon illumination at 700 nm, it converts to an unusual Pnr state ( $\lambda_{max} \sim 650$  nm) [37].

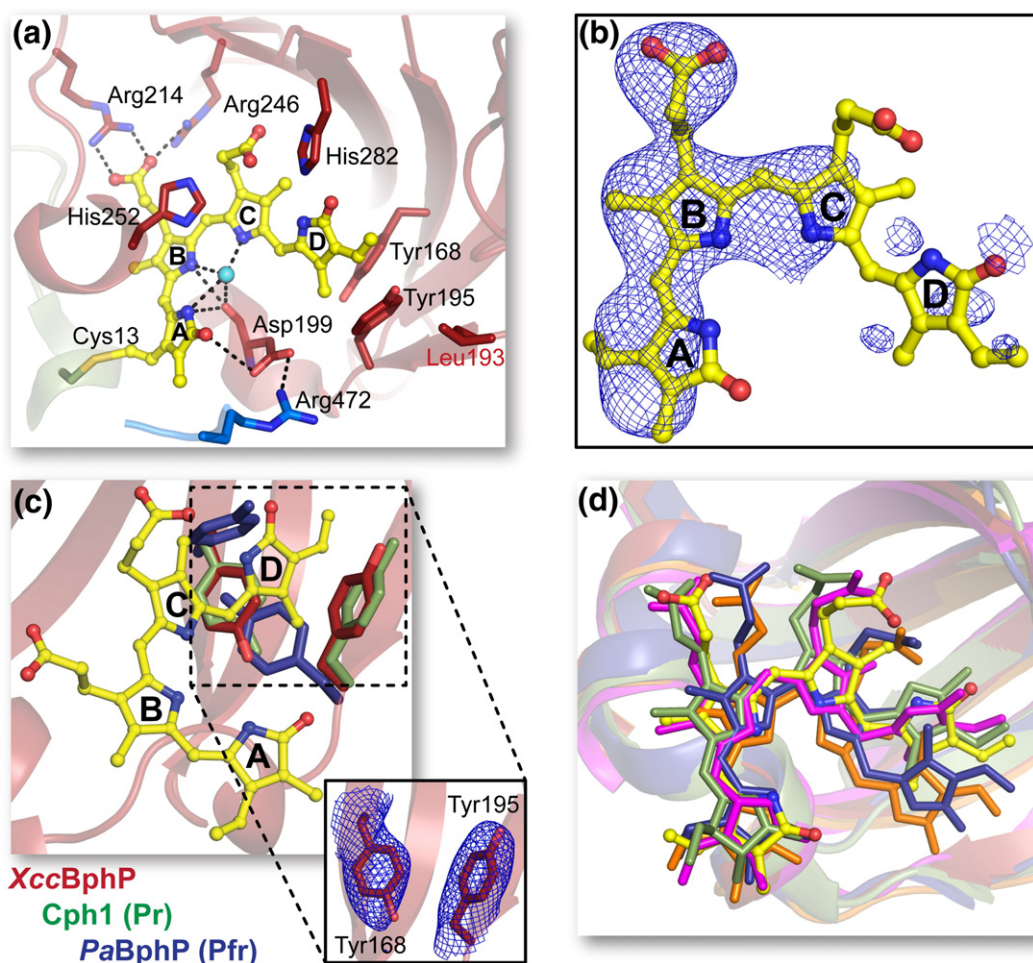


**Fig. 4.** Chromophore binding pocket. (a) Interaction of *XccBphP* with BV. The ligand is covalently bound to Cys13 (from the PAS2 domain) and buried into the GAF domain. BV is shown as capped sticks with carbon atoms in yellow, oxygen atoms in red, and nitrogen atoms in blue. The four pyrrolic rings are indicated as A, B, C, and D. The most relevant residues are depicted as sticks. A structural pyrrole water molecule is represented as a cyan sphere. Polar interactions are shown as dashed lines. The residue Leu193 (Gln188 from *PaBphP*) is labeled in red. (b) Feature-enhanced map [73] around BV, assuming a *ZZZssa* configuration. Weak electron density is seen at the region where the ring D is placed. The final  $2mF_o - DF_c$  electron density map is contoured at the 1.0  $\sigma$  level. (c) Tyrosine residues located next to ring D. Structural comparison between *XccBphP* (red) and representative BphPs in the Pr state (green, Cph1; PDB code 2VEA) and Pfr state (blue, *PaBphP*; PDB code 3C2W). The refined  $2mF_o - DF_c$  electron density map for both tyrosine residues is represented in the inset. (d) Structural contrast on the chromophore conformations buried into the GAF domains from *XccBphP*, *DrrBphP*-Pr state (magenta; PDB code 4O0P), Cph1-Pr state (green), *PaBphP*-Pfr state (blue), and *RpBphP1*-Pfr state (orange; PDB code 4GW9). The bilin chromophores are represented as sticks. BV in *XccBphP* is colored in yellow according to (a).

the C = C stretching mode of the C–D methine bridge of the protonated BV chromophore in the *ZZZssa* configuration (Pr) as demonstrated by the comparison with the RR spectrum of the Pr state in solution (Fig. 5a, bottom), and supported by quantum mechanics/molecular mechanics calculations (Fig. 5b). The corresponding mode of the A–B methine bridge may contribute to the broad feature at  $\sim 1655 \text{ cm}^{-1}$  (Fig. 5a, middle and bottom) although its exact position could not be determined due to the low signal-to-noise ratio. This is also true for the N-H in-plane bending, which is observed at  $1552 \text{ cm}^{-1}$  for Pr in solution. On the other hand, the broad bands at

$1584$  and  $1603 \text{ cm}^{-1}$  in the crystal spectra (Fig. 5a, middle) could not be related to Pr (or a *ZZZssa* chromophore). Instead they agreed with the corresponding bands of BV in the *ZZEssa* configuration which, in principle, might be Pfr (Fig. 5a, top) or its precursor Meta-R on the Pr  $\rightarrow$  Pfr conversion pathway [28], since both states exhibit a similar *ZZEssa* methine bridge geometry. The assignment to Meta-R appears to be more likely since (i) the RR spectrum of the crystals do not display any RR bands in the hydrogen-out-of-plane region, which are specifically characteristic only of Pfr but not of its precursor (Fig. 5a) [29], and (ii) it is consistent with a

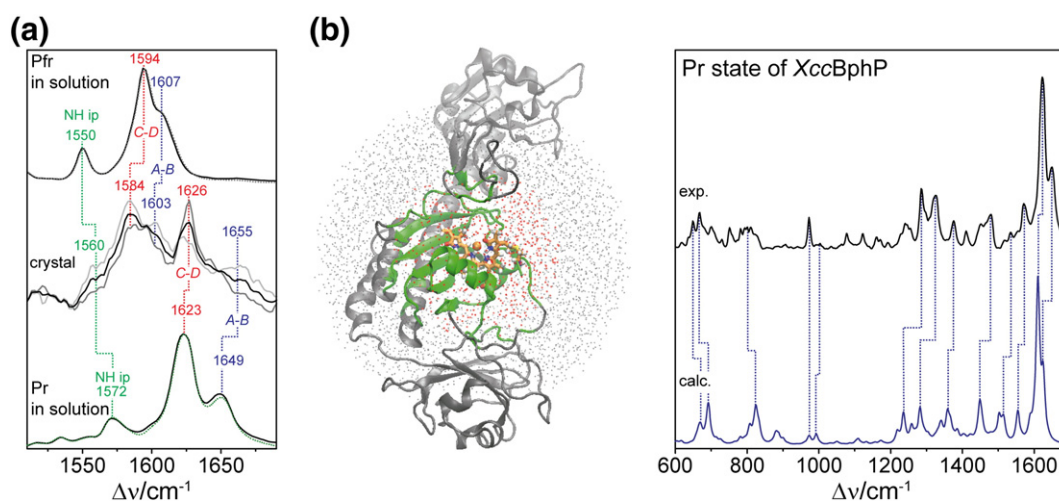


**Fig. 5.** Resonance Raman spectra of XccBphP and  $\Delta$ PAS9. (a) RR spectra of the Pfr state of XccBphP (black solid line) and  $\Delta$ PAS9 (dotted line) in solution (top), different XccBphP crystals (black, gray, and light gray lines) (middle) and the Pr state of XccBphP (black solid line) and  $\Delta$ PAS9 (dotted line) in solution (bottom). (b) QM/MM calculations on the XccBphP photosensory module. Left: QM/MM partition for the  $\Delta$ PAS9 structure solvated in a water sphere centered at ring C in the BV cofactor: atoms that do not belong to the active region are colored in gray. The colored regions comprising protein and water molecules represent the active QM/MM part, whereas the QM fragment is colored in orange. Right: experimental RR spectrum of the Pr state of XccBphP in frozen solution (top) and QM/MM calculated RR spectrum of the BV chromophore of XccBphP in the ZZZssa conformation (Pr) (bottom).

yet largely Pr-like structure of the chromophore pocket (*vide supra*, Fig. 4d) since the characteristic Pr-to-Pfr protein structural changes occur during the decay of Meta-R to Pfr [28]. Thus, the coexistence of two chromophore configurations, that is, ZZZssa (Pr) and ZZEssa (Meta-R), which differ in their C–D methine bridge geometry, can readily account for the lack of unambiguous electron density for ring D.

### XccBphP is a head-to-head dimer in the Pr conformation

In the crystal state, XccBphP forms a parallel head-to-head dimer where monomers are docked to each other in a left-handed shape, in agreement with other reported BphP crystal structures. A survey of possible quaternary assemblies using the PDBE-PISA server [30] suggests that this arrangement does not reflect a crystallization artifact but indeed represents a stable quaternary structure with a free energy gain of solvation ( $\Delta^{\dagger}G$ ) of  $-22.3 \text{ kcal mol}^{-1}$ . An extended interface area of approximately  $3200 \text{ \AA}^2$  is exclusively formed by long helical bundles across the PAS2, GAF, PHY, and PAS9 domains and is mainly stabilized by 22 salt-bridge interactions and 297 non-bonded contacts, involving  $\sim 15\%$  of the residues of the whole protein (Fig. 6a). Around 100 non-bonded contacts and four salt-bridge interactions are exclusively established between neighboring PAS9 domains and are lost in the  $\Delta$ PAS9 construct (Fig. 6b). To demonstrate the importance of these interactions, we performed SEC

coupled to static-light scattering (SLS) experiments using different constructs (Fig. 7). In this sense, XccBphP eluted at a lower volume (as a bigger particle) in the SEC in the dark and under different light sources, while both the isolated photosensory module and the PAS9 domain eluted at higher volumes (as smaller particles), respectively (Fig. 7a). Then, SLS measurements were used to calculate the apo-proteins or PAS9 domain molecular weights (MWs) revealing that it corresponds to a full-length XccBphP dimer, whereas both the PAS9 domain and  $\Delta$ PAS9 correspond to monomers (Fig. 7b). These findings demonstrate that the photosensory module and the PAS9 domain together in the full-length protein, but not individually, provide sufficiently strong interactions for dimer formation, thereby supporting, from an atomic point of view, previous suggestions on the role of the output module in dimerization [15,19,26,31–34]. A quaternary structural comparison between XccBphP, DrBphP (in Pr) [18], and PaBphP (in Pfr) [25] reveals a curved helical spine forming a gap at the parallel dimer interface that resembles the Pr state assembly (Fig. 8). However, this gap is less pronounced probably due to the high number of salt-bridge interactions, as described above.

Hence, the overall protein scaffold is characteristic of the Pr state as indicated by (i) the  $\beta$ -sheet tongue conformation found exclusively in all Pr state structures solved to date (Table 2); (ii) the presence of a leucine residue at position 193, which favors the Pr state in bathy phytochromes (Fig. 4a) [35]; (iii) the



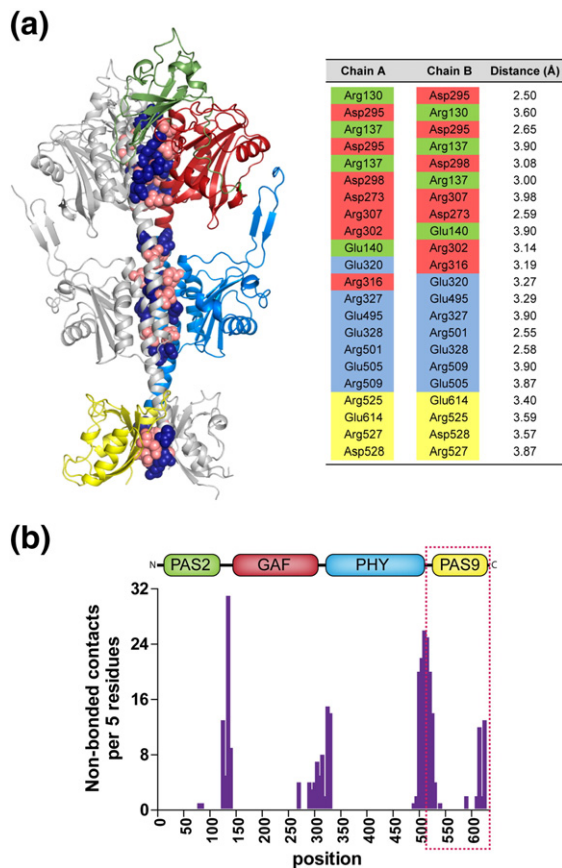


**Fig. 6.** Dimer interface of *XccBphP*. (a) Side view of salt-bridge contacts from side to side at the dimer interface (left). The PAS2, GAF, PHY, and PAS9 domains are depicted only for chain B. The charged residues stabilizing the dimer interface are colored shown as blue (Arg) and salmon spheres (Asp or Glu). Salt-bridge interactions between chains at the *XccBphP* dimer interface (4 Å cutoff, right). (b) Non-bonded contacts per five residues along the different domains. The contacts lost in the  $\Delta$ PAS9 construct are enclosed in the red-dashed box.

side chain conformation of the conserved Tyr168–Tyr195 pair that surrounds ring *D*, avoiding steric clashes (Fig. 4c); and (iv) the quaternary structure around the helical spine (Fig. 8c).

As a heterogeneous chromophore configuration (Pr/Meta-R) and a protein scaffold in a Pr state were found at the *XccBphP* crystals, these results can be reconciled by taking into account that, in solution, the Pfr and Pr states of *XccBphP* can be thermally converted into each other (*vide supra*, Fig. 2). These transformations start with the chromophore isomerization and are finalized by protein structural changes in the last step of the reaction pathway. Assuming that only the protein structural change associated with the Pr-to-Pfr transition is blocked in the crystalline state, the original Pfr/Pr equilibrium (85% Pfr versus 15% Pr, Fig. 2b) will be slowly

converted to a Pr/Meta-R equilibrium. Accordingly, one obtains a protein structure that is essentially characteristic of the Pr state and a distribution of the chromophore corresponding to a mixture of Pr and Meta-R configurations. This interpretation is consistent with the previous observation that the phototransformation of Pr crystals of the Agp1 phytochrome (*A. tumefaciens*) is arrested in the Meta-R state [28].

### Light-transducing elements of *XccBphP*

In order to get an initial insight into the light-driven conformational changes, we performed a limited trypsin proteolysis assay followed by mass spectrometry identification of the proteolytic products. We chose dark and far-red light conditions where Pfr or Pr conformations are enriched, respectively, as described above (Fig. 2b). The dark state sample underwent minimal proteolysis, consistent with a well-folded, compact protein (Fig. 9). In contrast, the far-red light-exposed sample was proteolyzed more quickly and extensively, with no intact full-length protein found after 30 min. Three differential fragments were found to be dependent on light exposure (Fig. 9). The first, with an approximate MW of 19.0 kDa (residues 131–302), comprises the GAF domain (red), indicating that light induces conformational changes in the linker regions N- and C-terminally to the GAF domain, increasing its exposure to the solvent. A second fragment (~18.0 kDa, residues 469–631/4) includes the C-terminal region of the PHY domain, starting from the loop of its tongue, and the PAS9 domain (blue). The result indicates that the latter loop is more solvent exposed under light conditions. This finding is in agreement with the already described conformational change of the tongue [18,24] (Table 2). The third fragment contains the PAS9 domain (yellow, residues 512 to 631/4, ~13.2 kDa). This observation indicates that the helical region N-terminally from the PAS9 domain undergoes a structural rearrangement as a consequence of the light-induced conformational changes of the sensor. We therefore suggest that this rearrangement represents the structural basis for the activation of the output module.

Unlike other phytochromes that harbor output modules with enzymatic function (i.e., HKs or c-di-GMP cyclase/phosphodiesterase), the C-terminal PAS9 module of *XccBphP* bears no known catalytic activity. Instead, signal transduction in *XccBphP* might occur *via* protein–protein interaction, as proposed for *RpbPhP1* [25], although the PAS9 domains from these two BphPs differ both in their tertiary structure ( $C^{\alpha}$ -r.m.s.d. = 2.81 Å; Table S2) and their role and orientation in dimerization. Additionally, PAS domains are well recognized to mediate interaction between proteins in signaling pathways [12].

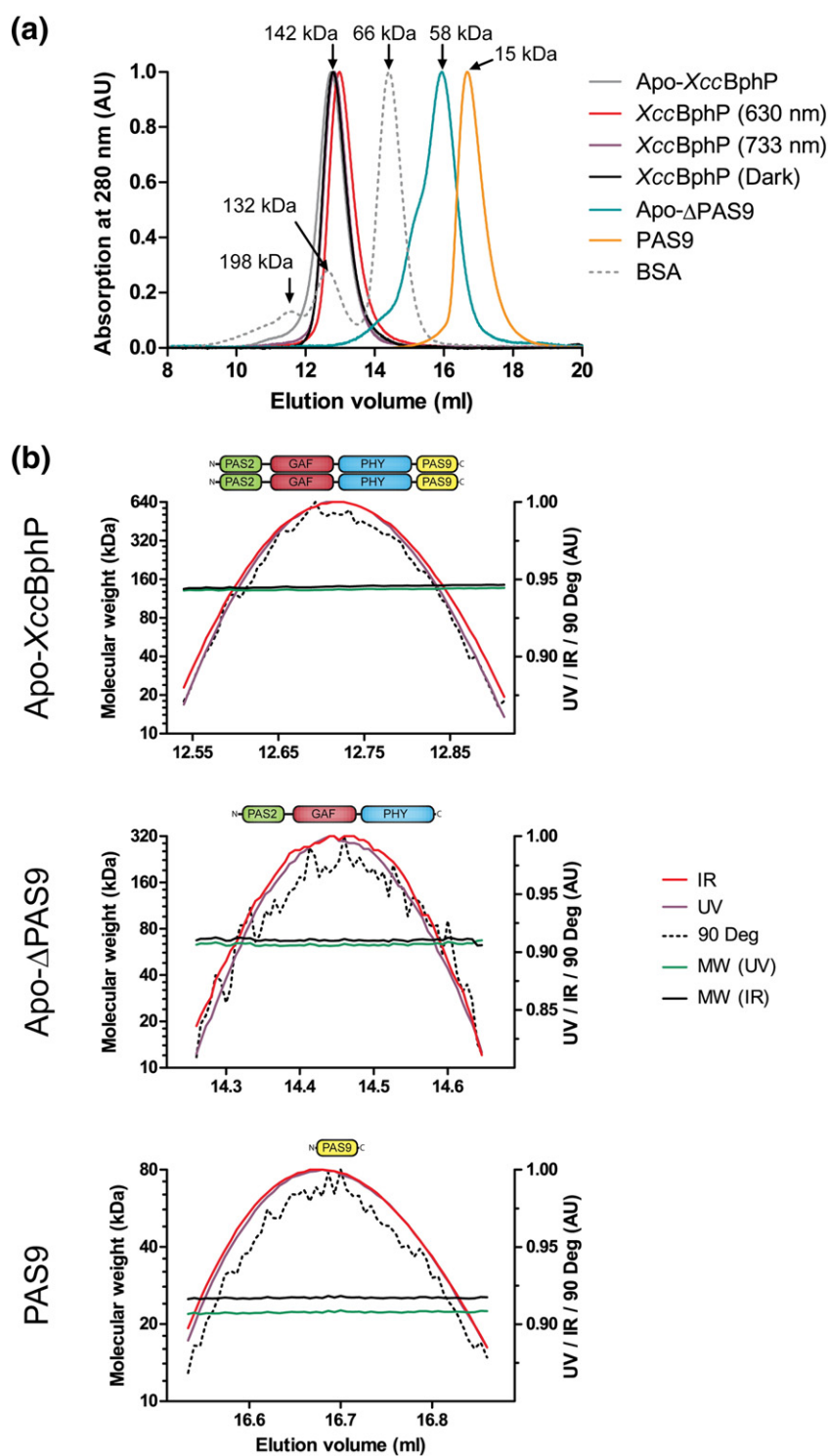


**Fig. 7.** SEC and SLS of *XccBphP*,  $\Delta$ PAS9, and PAS9. (a) Elution volumes were determined for the dark-adapted holoprotein (*XccBphP*) and for the illuminated protein with red (630 nm) or far-red light (733 nm), before and during the SEC runs. Apoproteins *XccBphP* (Apo-*XccBphP*) and  $\Delta$ PAS9, as well as the PAS9 domain were assayed and their MW calculated (black numbers). Theoretical MW for *XccBphP* dimer,  $\Delta$ PAS9 monomer, PAS9 monomer, and BSA control (monomer, dimer, and trimer) are indicated accordingly. (b) SEC-SLS measurement from Apo-*XccBphP* (top), Apo- $\Delta$ PAS9 (middle), and PAS9 (bottom). 90°, IR, and UV signals were employed for their MW determinations.

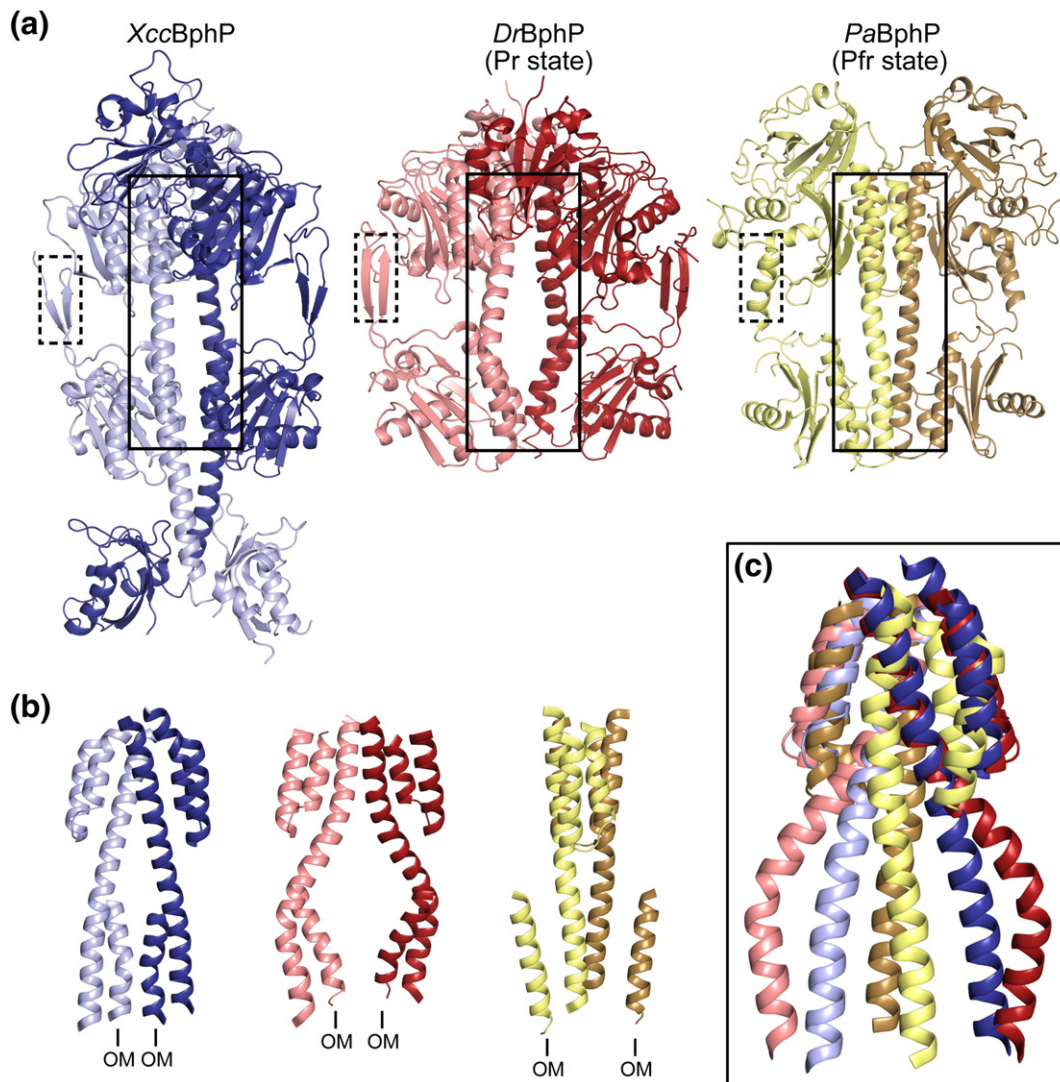


**Fig. 8.** Helical conformation at the dimer interface of *XccBphP*. (a) Quaternary structural comparison between *XccBphP* as Pr state (blue), *DrBphP* as Pr state (red; PDB code 4O0P), and *PaBphP* as Pfr state (yellow; PDB code 3C2W). The opposing monomers are displayed in darker colors. The helical spine and the tongue regions are highlighted in solid and dashed rectangles, respectively. (b) Detailed view of the helical interfaces. The C-terminal projections toward the output modules are indicated (OM). Views are rotated for clarity. (c) Structural alignment of the helical bundles from A. Only the three-helix bundle from the GAF domain and the GAF-PHY linker helix are shown.

## Discussion

### *XccBphP* long-range signal transduction model

In order to identify the structural features that are required for transmitting the signal in *XccBphP* from its photosensory core to the output module during the signal transduction, we compared the tertiary structures of *XccBphP* and *RpBphP1* (4GW9) due to the following reasons: (i) they are the only two available BphP crystal structures with a photosensory core harboring an output module; (ii) they share the same domain architecture (PAS2-GAF-PHY-PAS9),

with a sequence identity of 32% and the same output module (as *RpBphP1* structure lacks an unstable 10-kDa C-terminal HOS domain); (iii) both proteins are bathy (-like) phytochromes; and (iv) these two structures correspond to different states (*XccBphP*, Pr and *RpBphP1*, Pfr). The pairwise alignment between *XccBphP* and *RpBphP1* shows that the *XccBphP* helical spine is curved leading to a displacement of the output module by  $\sim 30^\circ$  with respect to the photosensory module, while in *RpBphP1* the helical spine is fairly straight (Fig. 10a and b). This structural rearrangement is not likely to be artifactually caused by the crystallization conditions or by neighboring interactions that could bend the molecule as both

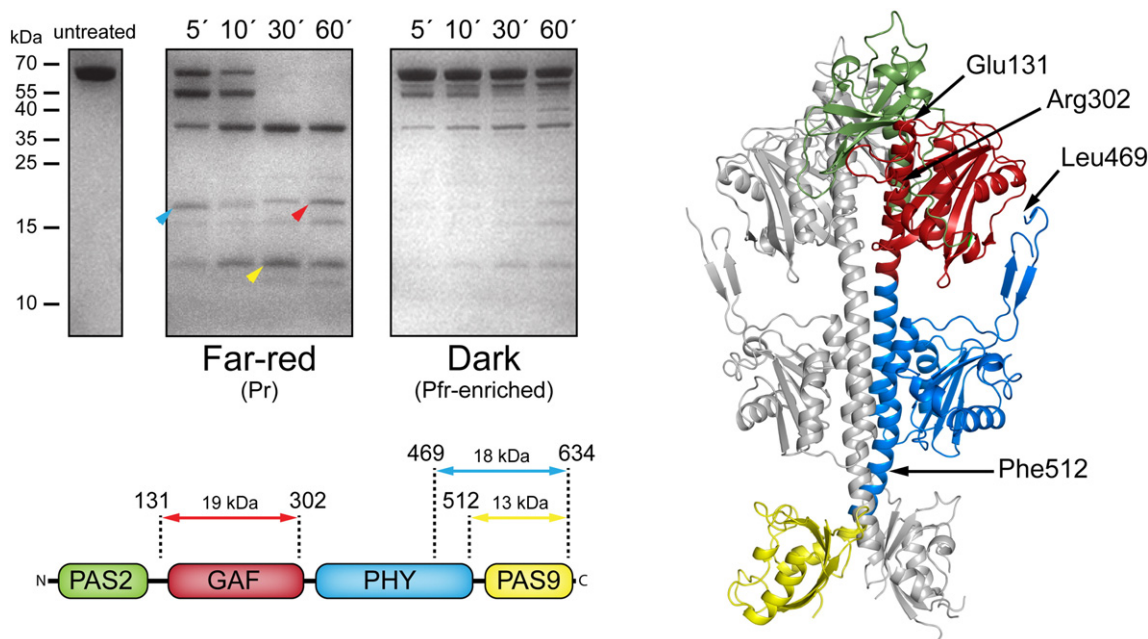


**Fig. 9.** Light-induced conformational changes in XccBphP. Far-red light or dark-treated XccBphP differential fragments after limited proteolysis identified by SDS-PAGE-mass spectrometry are indicated by colored arrows. Light treatment generates three fragments of ~19.0 kDa (residues 131–302, GAF domain, red), ~18.0 kDa (residues 469–631/4, PHY domain starting from the loop of the tongue, blue), and ~13.2 kDa (PAS9 domain, yellow). Untreated: no addition of trypsin. MW standards and incubation times are indicated. Domain architecture scheme showing the fragments identified (bottom left). The cleavage sites that generate these fragments are mapped in the structure (right).

PAS9 domains in the XccBphP dimer are relatively open in the crystal packing (Fig. S2). Therefore, the displacement may be the consequence of the different tongue conformations observed in both structures, that is,  $\beta$ -sheet (Pr protein structure) in XccBphP and  $\alpha$ -helix (Pfr protein structure) in RpbphP1 (Fig. 10c). In the Pr state of XccBphP, the BV chromophore may assume a ZZZssa configuration (Fig. 10c, left), while RpbphP1 in the Pfr state of RpbphP1 displays a rotated bilin ring D, adopting a ZZEssa configuration (Fig. 10c, right). Recently, Takala *et al.* reported how these conformational changes around the chromophore are involved in the different tongue configurations during photoconversion [15]. In this fashion, they uncovered that the Pr–Pfr conversion implies a  $\beta$ -sheet-to- $\alpha$ -helix tongue refolding, inducing a shortening of this peptide segment, which can be reversibly switched. Taking this into account, we propose that the tertiary structure of the Pr state of XccBphP can be converted to a Pfr state similar to the one described for RpbphP1: these Pr-to-Pfr structural changes in the tongue may pull the PHY domain toward the GAF domain, straightening the helical spine linker (Fig. 10d), similarly as previously reported for other BphPs [15,18,32]. The reverse Pfr-to-Pr process may consequently push the PHY domain away from the GAF domain, causing the bending of the helical spine. Straightening and bending of the helix linker may induce a reorientation of the output module, such that it

may either allow or impair interactions with the respective partner protein of the downstream signaling process (Fig. 10d). In fact, a change in the XccBphP secondary structure from  $\alpha$ -helix (Pfr) to  $\beta$ -sheet (Pr), albeit relatively small, is clearly detected in the “Pr-minus-Pfr” IR difference spectrum and readily assigned to the structural change of the tongue (Fig. 10e), as previously demonstrated [16,36]. The limited proteolysis experiments on Pr (far-red) and Pfr-enriched (dark adapted) XccBphP are consistent with this model where the tongue and the helical spine hinge regions were identified as elements that suffer from conformational changes upon illumination. Furthermore, the long-range signaling model proposed for XccBphP also supports earlier suggestions about the coupling between the tongue region from the photosensor and the HK output module *via* the helical dimer interface [19,24,26,31] and thus might hold for other phytochromes, regardless of the nature of their output modules.

### Parallel versus antiparallel dimers

To finish, although most BphP structures share similar tertiary architectures and low r.m.s.d. values for their monomers, quite different quaternary arrangements (i.e., head-to-tail or head-to-head) have been found, as recently reported for the RpbphP2 and RpbphP3 structures [37]. However,

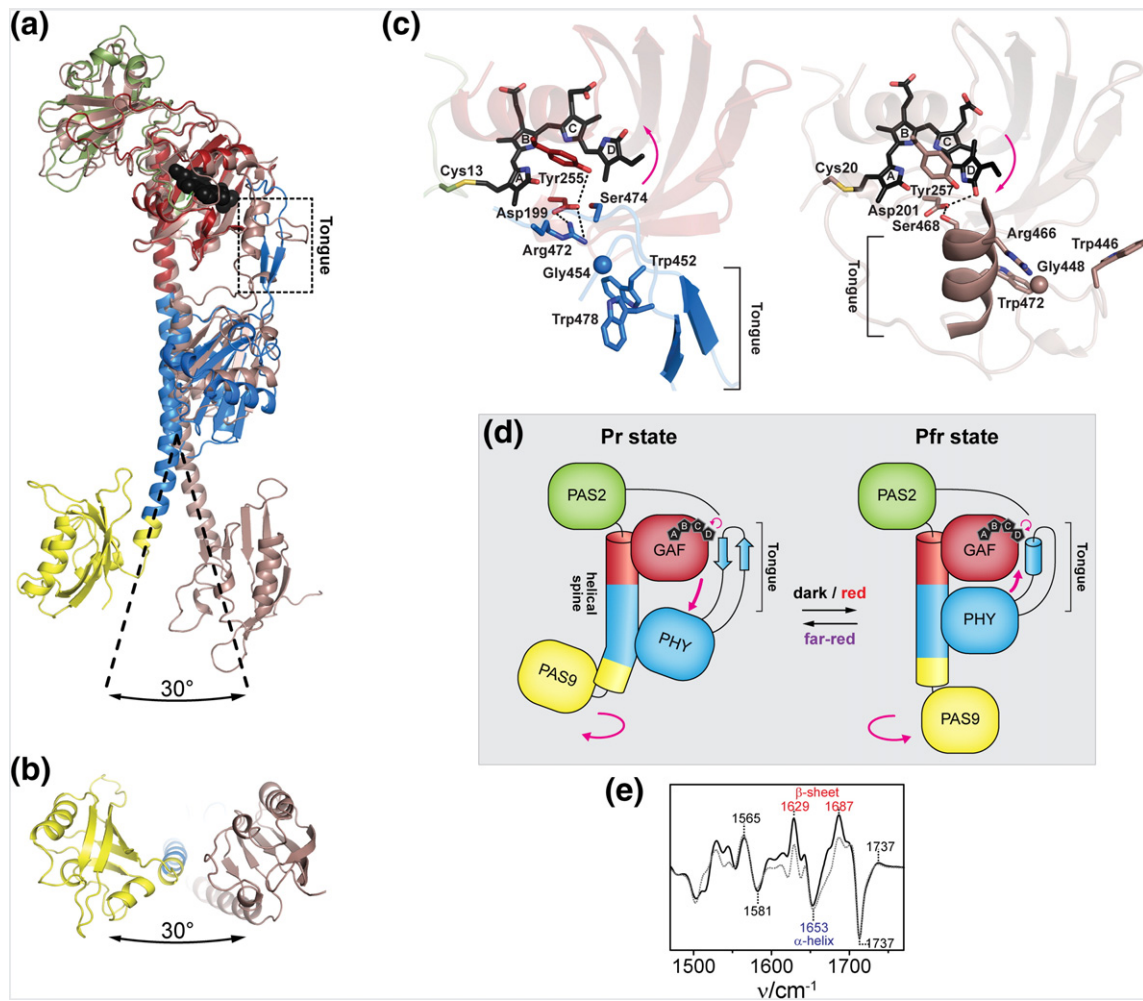


**Fig. 10.** Proposed structural rearrangements upon *XccBphP* photoconversion. (a) Tertiary structural contrast between the Pr state of *XccBphP* and the Pfr state of *RpBphP1* from *R. palustris* (dark salmon; PDB code 4GW9). The orientation change of the helical spine is indicated. The tongue region is boxed in a dashed rectangle. BV is shown as black spheres. (b) Bottom view of the output modules from (a). (c) Chromophore surroundings in *XccBphP* in Pr (left) and *RpBphP1* in Pfr (right). Relevant conserved amino acids are shown as sticks with carbon atoms colored according to (a), oxygen atoms (red), nitrogen atoms (blue), and sulfur atoms (yellow). The chromophore ring D movements upon photoconversion are represented with magenta arrows. BV is shown as black capped sticks, and the pyrrolic rings are indicated as A, B, C, and D. Salt bridges and hydrogen bonds are depicted as dashed lines. The view is rotated a few degrees with respect to (a). (d) Proposed model for the structural rearrangements in full-length *XccBphP* upon photoconversion. The output module adopts different orientations in each state, caused by bending or straightening of the helical spine. The magenta arrows indicate the isomerization of the chromophore ring D and the reorientations of the PHY and PAS9 domains. The tongue region is indicated and the pyrrolic rings from BV are shown as black pentagons with the letters A, B, C, and D. (e) IR difference spectra of *XccBphP* and  $\Delta$ PAS9. "Pr-minus-Pfr" of *XccBphP* (black solid line) and  $\Delta$ PAS9 (dotted line).

in both arrangements, their interfaces are mostly packed by helical bundles between the same or different intermolecular domains, respectively. The *RpBphP1* dimer assembly has been captured showing an antiparallel head-to-tail arrangement, where only the C-terminal regions from opposing chains are interlocked in the dimer interface [25]. While this unusual quaternary organization has been proposed to be functional for this particular phytochrome, there are strong arguments that the parallel dimer arrangement, as found in *XccBphP*, represents

the biologically relevant quaternary assembly of BphPs in general: (i) this arrangement is advantageous when the output modules need to work in concert [38], (ii) most BphPs as well as the plant phytochrome PhyB [39] adopt three-dimensional structures that form parallel scaffolds, (iii) long helices implicated in signal propagation are mostly arranged in a parallel fashion [40–42], and (iv) crystal structures containing the HK module generally adopt a parallel assembly [43–48]. Moreover, small angle X-ray scattering [24] and single-particle cryoelectron

microscopy [31,32] have provided evidence that phytochromes function in a parallel head-to-head arrangement. Nevertheless, more full-length BphP structures are clearly required to get a broader landscape regarding the various output module organizations into the dimer interface in different photostates.

## Concluding Remarks

It has been proposed that the tongue interconversion between the  $\alpha$ -helix and  $\beta$ -sheet forms, after BV photoconversion within the photosensory module, may cause rotational movements in the main helical spine. Integrating previous findings with the structural data reported here, a simple model for signal propagation from the photosensory core to the output module for XccBphP is proposed. This structural analysis suggests that the refolding of the tongue, as well as the pull/push displacement between the GAF and PHY domains, previously reported in the Pr–Pfr switch, may provoke a kink and a rotation of the output module position during the XccBphP photoconversion mechanism. These long-range rearrangements in the output module positioning may elicit the biological signaling cascade. Moreover, the XccBphP crystal structure confirms the parallel dimerization model previously proposed for other full-length phytochromes [31,32]. To finish, helical connectors between sensory and output modules found among natural and artificial photoreceptors have already been proposed as transducing elements [38,48–51]. For these reasons, the long-range signal transmission mechanism model presented in this work may contribute to the common understanding of photoreception.

## Materials and Methods

### Bacterial strains and culture conditions

*Escherichia coli* strains were cultured at 37 °C in Luria–Bertani medium. When required, the antibiotics kanamycin (Km), chloramphenicol (Cm), and ampicillin (Amp) were added in final concentrations of 35, 25, and 100  $\mu\text{g mL}^{-1}$ , respectively.

Strains, plasmids and oligonucleotides are presented in Table S1.

### Generation and purification of XccBphP, $\Delta$ PAS9, and PAS9 recombinant proteins

XccBphP (residues 1–634),  $\Delta$ PAS9 (residues 1–511), and PAS9 (residues 517–634) fragments were amplified from the XC\_4241 ORF using *X. campestris* pv. *campestris* strain 8004 genomic DNA, Platinum Pfx DNA Polymerase (Life Technologies) and specific primers BphP\_F–BphP\_R, BphP\_F– $\Delta$ PAS9\_R, and PAS9\_F–BphP\_R, respectively.

Amplicons were cloned into the NdeI/BamHI restriction sites of the pET24A vector (Novagen) to generate pET-XccBphP, pET- $\Delta$ PAS9, and pET-PAS9. The three constructs include a six-residue long histidine tag at their N-termini.

*E. coli* BL21(DE3)pLysE cells were transformed with the resulting vectors. Cultures were induced with a final concentration of 0.4 mM IPTG overnight at 20 °C with agitation at 250 rpm. Cells were harvested and ruptured. Next, proteins were purified as previously described [14]. Holoproteins were produced by incubation of the apo-proteins for 1 h at room temperature in the presence of BV (Sigma-Aldrich) and then subjected to SEC. Protein concentrations were estimated using the calculated molar extinction coefficient  $\epsilon$  at 280 nm provided by the ExpASy ProtParam tool [52] based on the polypeptide sequence for the monomer ( $\epsilon_{\text{XccBphP}} = 74,370$ ,  $\epsilon_{\Delta\text{PAS9}} = 64,400$ ,  $\epsilon_{\text{PAS9}} = 9970 \text{ M}^{-1} \text{ cm}^{-1}$ ). When necessary, the contribution from BV was subtracted.

### Crystallization, data collection, and processing

Crystals of full-length XccBphP in the presence of BV were grown from solutions containing 0.1 M Tris (pH 8.3), 12% (w/v) PEG 4000, and 0.2 M sodium acetate, as previously described [14]. Samples were cryoprotected by a quick soak in the crystallization solution added with 25% (w/v) PEG 400. Setting up of the drops was performed under dim ambient light. Crystallization trays were kept in the dark covered in aluminum foil. For the visualization of the drops and manipulation of the crystal samples for cryo-cooling, minimal exposure to microscope light was applied using a green filter (passband: 450–600 nm, low-pass cut-off: 770 nm) (LEE Filters, Hampshire, UK). The best X-ray diffraction data set was collected at the PROXIMA 1 protein crystallography beamline at the SOLEIL synchrotron (France) at 3.25 Å resolution, using a PILATUS 6M detector (Dectris, Baden, Switzerland). This data set was 100% complete, with an  $R_{\text{pim}}$  factor of 4.2% (52% in the last shell) and a mean  $\langle I/\sigma(I) \rangle$  of 2.4 at the highest resolution shell (Table 1). Diffraction data were processed using XDS [53] and scaled using SCALA from the CCP4 program suite [54], isolating 5% of the measured reflection for cross-validation purposes. The crystals belong to the tetragonal space group  $P4_32_12$ , with unit-cell parameters  $a = b = 103.94$ ,  $c = 344.57$  Å. Analysis of the Matthews coefficient [55] suggested the presence of two chains in the asymmetric unit with a solvent content of approximately 62%.

### Structure determination, model building, and refinement

A partial XccBphP structure was obtained by molecular replacement method with the program PHASER [56] using the atomic coordinates of RpBphP1 as template (PDB code 4GW9; 28% sequence identity for 613 aligned residues). The preliminary model was refined as a rigid body with the program BUSTER-TNT getting less than 50% of the residues at the asymmetric unit correctly positioned and  $R_{\text{factor}} = 49\%$ ). Subsequently, the main chain was fixed in the density using strict geometry restraints and the incomplete regions were manually traced in COOT [57] adding alanine residues as first attempt. Due to the low

resolution, three-dimensional models belonging to different structural homologs of the individual domains were used as templates during this process (PDB codes 4GW9, 2VEA, 3NHQ, and 3T50). At this step, density modification with the program PARROT from CCP4 was crucial to get an improved  $2mF_o - DF_c$  electron density map. After several cycles of refinement using BUSTER [58] with NCS, TLS, and automatic low resolution restraints, the partial model showed a promising  $R_{\text{factor}}$  of 36%. After this step, restraints were switched off, and further refinement and manual building cycles were performed until completion of the final model, which displayed very good statistics with  $R_{\text{work}}/R_{\text{free}}$  values of 20.5/25.5% and favorable stereochemistry (Table 1).

### Validation, analysis, and graphical representation of the model

The final model was subjected to validation with MolProbity [59] as well as with the validation module implemented in COOT. The following Web servers at the European Bioinformatics Institute were used: PDBePISA (study of interface areas<sup>‡</sup>) [30], PDBeFold (superposition and r.m.s.d. calculations<sup>§</sup>) [60], LigPlot + (protein–ligand interactions<sup>||</sup>) [61], PDBsum (topology analysis<sup>¶</sup>) [62], and ClustalO (protein sequences alignment<sup>\*\*</sup>) [63]. Protein domains were determined with the Pfam server<sup>‡‡</sup> [64]. Molecular structures and their electron densities were represented using PyMOL [65]. The protein topology diagrams were drawn using the TopDraw software from the CCP4 suite.

### UV–Vis spectroscopy and curve fitting

Holoprotein solutions containing 1 mg mL<sup>-1</sup> of XccBphP or ΔPAS9 in 50 mM Tris–HCl and 250 mM NaCl (pH 7.7; buffer A) were irradiated with a red (630 nm) 1 W LED or far-red (733 nm) 0.7 W LED for 10 min. Absorption spectra were collected in an 8452A diode array spectrometer (Hewlett Packard). The dark states were determined after proteins were kept in the dark for 96 h. Dark assembly experiments were performed adding BV in the dark (2:1 molar ratio) to a 1 mg mL<sup>-1</sup> apoprotein solution of XccBphP or ΔPAS9 in buffer A. The reaction was followed by absorption spectra determination. Dark recovery experiments were performed by irradiating XccBphP and ΔPAS9 holoprotein solutions and recording the absorption spectra periodically in a time period of 21 h at room temperature.

XccBphP dark and red experimental absorption spectra in the range 340–820 nm were fitted according to Eq. (1):

$$\text{Abs}(\lambda) = \alpha \cdot \text{Abs}_{\text{Pr}}(\lambda) + \beta \cdot \text{Abs}_{\text{Pfr}}(\lambda) \quad (1)$$

where  $\text{Abs}_{\text{Pr}}(\lambda)$  represents the absorption value in each wavelength from the far-red illuminated Pr state and  $\text{Abs}_{\text{Pfr}}(\lambda)$  from the ΔPAS9 dark-adapted state, which shows minimal Pr contribution. Amplitudes  $\alpha$  and  $\beta$  were the parameters fitted. Pr and Pfr ratios were calculated according to Eqs. (2) and (3):

$$\text{Pr}_{\text{ratio}} = \frac{\sum \alpha \cdot \text{Abs}_{\text{Pr}}(\lambda)}{\sum \text{Abs}(\lambda)} \quad (2)$$

$$\text{Pfr}_{\text{ratio}} = \frac{\sum \beta \cdot \text{Abs}_{\text{Pfr}}(\lambda)}{\sum \text{Abs}(\lambda)} \quad (3)$$

For the dark recovery experiments, exponential functions were fitted to the absorbance change at 752 nm according to Eqs. (4) and (5) for XccBphP and ΔPAS9, respectively:

$$\text{Abs}_{752}(t) = A - B \cdot e^{-t \cdot C} \quad (4)$$

$$\text{Abs}_{752}(t) = D - E \cdot e^{-t \cdot F} - G \cdot e^{-t \cdot H} \quad (5)$$

The Pfr contribution as a function of time (%) was calculated according to Eq. (6):

$$\text{Pfr}(t) = \frac{\text{Abs}_{752t} - \text{Abs}_{752t0}}{\text{Abs}_{752t \rightarrow \infty} - \text{Abs}_{752t0}} \cdot \text{Pfr}_{\text{ratio} 96\text{h}} \cdot 100 \quad (6)$$

For dark conversion, the half-time was estimated as the time in which 50% of the Pr-to-Pfr conversion took place considering the saturation value as 100%.

### RR and IR measurements

XccBphP RR spectra were recorded following the procedures reported previously [16]. RR measurements of single protein crystals were performed using a Raman-scope III Raman microscope connected to an RFS-100 FT-Raman spectrometer (Bruker Optics) via an optical fiber. The laser power of the 1064-nm excitation line was set to 200 mW at the sample. XccBphP crystals containing a thin layer of crystallization buffer were shocked-frozen in liquid nitrogen prior to spectra recording, carried out according to the previously described procedure [28]. Measurements were performed in an IFS-28 infrared spectrometer (Bruker Optics) equipped with a home-built cryostat. Further details are given elsewhere [16].

### Quantum mechanics/molecular mechanics calculations

Computational refinement of the chromophore binding site of the experimental crystal structure was done using a well-established approach combining MD simulations with hybrid quantum mechanics/molecular mechanics (QM/MM) calculations [29,66]. The all-atom MD simulations of XccBphP were performed taking as initial coordinates those from the photosensory domain of chain B of the crystallographic structure (residues 12–500). Hydrogen atoms were added to this structure via the HBUILD routine implemented in the CHARMM 32b2 software [67]. The protonation state of the titratable side chains was chosen upon visual inspection of their environments. In particular, all histidine residues, except for His107, His231, His282, His283, His365, His372, and His493, were protonated at their  $\delta$ -nitrogen atom. According to the RR experiments, the tetrapyrrole chromophore is protonated at the ring B and C nitrogen atoms, whereas the propionic side chains are deprotonated yielding a total charge of  $-1e$ . To account for the elongated shape of the protein, a hexagonal box of TIP3P water containing water molecules was chosen for solvating the XccBphP monomer. This model system was relaxed by performing a

series of energy minimizations followed by 15-ns MD simulations using the CHARMM27 force field for the protein and water and the NAMD software [68]. Due to the lack of accurate internal MM force field parameters for bilin cofactors, the BV molecule was held fixed during all MD simulation steps. Furthermore, in order to avoid large structural deviations with respect to the crystal structure, all Ca atoms were restrained to their original positions.

The resulting MD-equilibrated structure was taken as input for the subsequent QM/MM geometry optimization step, which was performed with the modular package Chemshell [69]. Here, the geometry of the BV cofactor was optimized together with its immediate protein environment defined by all residues within a 20-Å sphere centered at the nitrogen atom of ring C. In the QM region, we included the BV molecule, the side chain of Cys13, and the pyrrole water. All these atoms were described with density functional theory at the B3LYP/6-31G\* level. The remaining atoms (the so-called “active MM part”) were treated with the empirical CHARMM27 force field. The coupling between QM and MM regions was computed using the electrostatic embedding approach combined with a charge shifted scheme [70].

Finally, the vibrational frequencies and Raman intensities of the QM fragment were computed by conventional normal mode analysis following the procedure described elsewhere [66]. Hessian matrix and polarizability derivatives were computed with the Gaussian 09 software [71]. In order to partially correct for intrinsic errors associated with the harmonic approximation and systematic deficiencies of the DFT approach, the QM force constants were scaled with a global set of scaling factors according to the procedure developed by Rauhut and Pulay [72]. For the presentation of the Raman spectrum, the bandshapes of the individual modes were described by Lorentzian functions using a full width at half height of 12 cm<sup>-1</sup>.

### SEC-SLS measurements

The average MWs of XccBphP, ΔPAS9, and PAS9 were determined using a PD2010 90° light scattering instrument (Precision Detectors) connected in tandem to a high-performance liquid chromatography system (HPLC), an LKB 2142 Differential Refractometer Detector (Pharmacia), and a 486 Tunable Absorbance Detector (Waters). Only MWs for apoproteins could be calculated due to the interference produced by BV in the 90° light scattering measurements because of its absorption in the laser wavelength (685 nm, AlGaInP). A Superdex 200 HR-10/30 column (24 mL; GE Healthcare Life Sciences) was used with isocratic elution in Tris-HCl and 250 mM NaCl (pH 7.7) at a flow rate of 0.4 mL min<sup>-1</sup> at 20 °C, with 0.1 mg of injected protein sample. The MW was calculated relating its 90° to the IR or UV signals using the software Discovery32 supplied by Precision Detectors with BSA (MW 66.5 kDa) as a standard. Apoproteins XccBphP and ΔPAS9, as well as the PAS9 domain were assayed under normal laboratory conditions. To determine the elution volumes, the XccBphP holoprotein was dark-adapted and subjected to HPLC, with the column covered with two layers of aluminum foil. Light treatments were performed illuminating XccBphP with red or far-red light: (i) the protein samples for 10 min before the injection and (ii) the column during the HPLC run.

### Limited proteolysis

Dark-adapted holo-XccBphP samples were used for limited proteolysis. A 1:500 ratio (w/w) of trypsin (Sigma-Aldrich, T1426) to protein was used in 5% glycerol. The dark-adapted protein was pre-illuminated for 30 min with far-red light or kept under dark conditions. Then, trypsin was added and after 5, 10, 30, and 60 min, the reactions were stopped by the addition of SDS loading buffer containing 25% glycerol. Samples were visualized in 20% SDS-PAGE gels using Tris-Tricine running buffer. Excised protein bands resulting from the different partial tryptic digestions in different conditions were washed successively with (i) 50 mM ammonium bicarbonate, (ii) 25 mM ammonium bicarbonate–50% acetonitrile, and (iii) 100% acetonitrile. Then bands were reduced and alkylated using 10 mM DTT and 100 mM iodoacetamide, and in-gel digested with 100 ng of trypsin in 25 mM ammonium bicarbonate overnight at 37 °C. Tryptic peptides were recovered by elution with 50% acetonitrile–0.5% trifluoroacetic acid, including brief sonication, and further concentrated by speed-vacuum drying. Samples were resuspended in a minimum volume of 50% acetonitrile and 0.5% trifluoroacetic acid. Each sample was mixed 1:1 with 3 mg mL<sup>-1</sup> α-cyano-4-hydroxycinnamic acid and spotted onto a MALDI target for co-crystallization.

MS data were collected in an Ultraflex II Bruker Daltonic MALDI TOF/TOF equipment and acquired in Reflectron positive mode using a detection mass range of 700 to 4000 Da, where 1250 laser shots were averaged for each mass spectrum. The equipment was calibrated with Bruker calibrant mixture Pep Mix II. The peak list was generated based on signal-to-noise filtering and using an exclusion list of contaminants. Peaks observed in the different MS lists were compared to the masses of the theoretical peptides originated in a protein sequence *in silico* digestion. The matching peptides were validated by MS/MS fragmentation when possible.

The digests were also analyzed by Nano LC-MS/MS in a Thermo Scientific Q Exactive Mass Spectrometer. A 40-min gradient of H<sub>2</sub>O:ACN at a flow of 33 nL min<sup>-1</sup> was used with a C18, 2 μm, 100A column, and a Data-dependent MS2 method was used to fragment the top 12 peaks in each cycle. The partial proteolysis products were also analyzed by MS, without further tryptic digestion, to determine the intact mass of each proteolysis product. Samples were mixed 1:1 with 10 mg mL<sup>-1</sup> sinapinic acid and spotted onto a MALDI target for co-crystallization. The data were acquired in linear and reflectron mode from a mass range of 10 to 100 kDa, where 1250 laser shots were averaged for each mass spectrum. The equipment was calibrated with Bruker calibrant mixture ProtCallI.

All the combined information was used to map the proteolytic peptides generated in each condition. Protein digestion and MS analysis were performed at the Proteomics Core Facility CEQUIBIEM, University of Buenos Aires, Argentina.

### Accession numbers

Coordinates and structure factors have been deposited in the Protein Data Bank with accession number 5AKP.



## Acknowledgments

This work was supported by the Argentinian Ministry of Science (MINCyT), the Argentinian Research Council (CONICET), and the National Agency for the Promotion of Science and Technology of Argentina (ANPCYT) grant PICT 2011-2672. Support by the Deutsche Forschungsgemeinschaft (Sfb1078) is gratefully acknowledged (B6, P.H.; C3, M.A.M.). We are grateful for the access to the PROXIMA 1 beamline at the SOLEIL synchrotron, France. We thank Dr. Winslow Briggs and Dr. Roberto Bogomolni for revising the manuscript.

**Author contributions:** J.R., F.V.E., M.A.M., F.A.G., and H.R.B. conceived or designed the experiments; S.K., J.R., F.V.E., M.F.L., M.A.M., and H.R.B. performed the experiments; L.H.O., S.K., J.R., F.V.E., M.A.M., F.M., A.A.V., P.H., and H.R.B. analyzed data; and L.H.O., J.R., P.H., and H.R.B. wrote the paper.

### Conflicts of interest:

The authors declare that they have no conflicts of interest with the contents of this article.

## Appendix A. Supplementary data

Supplementary data to this article can be found online at <http://dx.doi.org/10.1016/j.jmb.2016.04.012>.

Received 13 January 2016;  
Received in revised form 6 April 2016;  
Accepted 8 April 2016  
Available online 20 April 2016

### Keywords:

*Xanthomonas campestris* pv. *campestris*;  
phytochrome;  
biliverdin;  
red-light photoreceptor;  
signal transduction

†Bonomi H.R. *et al.*, manuscript in preparation.  
‡[www.ebi.ac.uk/msd-srv/prot\\_int](http://www.ebi.ac.uk/msd-srv/prot_int)  
§[www.ebi.ac.uk/msd-srv/ssm](http://www.ebi.ac.uk/msd-srv/ssm)  
||[www.ebi.ac.uk/thornton-srv/software/LigPlus](http://www.ebi.ac.uk/thornton-srv/software/LigPlus)  
¶[www.ebi.ac.uk/pdbsum](http://www.ebi.ac.uk/pdbsum)  
‡†[www.ebi.ac.uk/Tools/msa/clustalo](http://www.ebi.ac.uk/Tools/msa/clustalo)  
‡‡<http://pfam.xfam.org>

### Abbreviations used:

BphP, bacteriophytochrome; BV, biliverdin IX $\alpha$ ; GAF, cGMP phosphodiesterase/adenylate cyclase/FhlA transcriptional activator; HK, histidine kinase; MD, molecular dynamics; OM, output modules; PAS, Period/ARNT/Single-minded; Pfr, far-red-absorbing; PHY, phytochrome specific; QM/MM, quantum mechanics/molecular mechanics; SLS, static-light scattering; *Xcc*, *Xanthomonas campestris*

pv. *campestris*; XccBphP, *Xanthomonas campestris* pv. *campestris* bacteriophytochrome.

## References

- [1] T.E. Swartz, T.S. Tseng, M.A. Frederickson, G. Paris, D.J. Commerci, G. Rajashekara, et al., Blue-light-activated histidine kinases: two-component sensors in bacteria, *Science* 317 (2007) 1090–1093.
- [2] H.R. Bonomi, D.M. Posadas, G. Paris, C. Carrica Mdel, M. Frederickson, L.I. Pietrasanta, et al., Light regulates attachment, exopolysaccharide production, and nodulation in *Rhizobium leguminosarum* through a LOV-histidine kinase photoreceptor, *Proc. Natl. Acad. Sci. U.S.A.* 109 (2012) 12135–12140.
- [3] I. Kraiselburd, A.I. Alet, M.L. Tondo, S. Petrocelli, L.D. Daurelio, J. Monzon, et al., A LOV protein modulates the physiological attributes of *Xanthomonas axonopodis* pv. *citri* relevant for host plant colonization, *PLoS One* 7 (2012), e38226.
- [4] N.C. Rockwell, Y.S. Su, J.C. Lagarias, Phytochrome structure and signaling mechanisms, *Annu. Rev. Plant Biol.* 57 (2006) 837–858.
- [5] N.C. Rockwell, D. Duanmu, S.S. Martin, C. Bachy, D.C. Price, D. Bhattacharya, et al., Eukaryotic algal phytochromes span the visible spectrum, *Proc. Natl. Acad. Sci. U.S.A.* 111 (2014) 3871–3876.
- [6] G. Rottwinkel, I. Oberpichler, T. Lamparter, Bathy phytochromes in rhizobial soil bacteria, *J. Bacteriol.* 192 (2010) 5124–5133.
- [7] M.E. Auldridge, K.T. Forest, Bacterial phytochromes: more than meets the light, *Crit. Rev. Biochem. Mol. Biol.* 46 (2011) 67–88.
- [8] R.D. Vierstra, J. Zhang, Phytochrome signaling: solving the Gordian knot with microbial relatives, *Trends Plant Sci.* 16 (2011) 417–426.
- [9] S.J. Davis, A.V. Vener, R.D. Vierstra, Bacteriophytochromes: phytochrome-like photoreceptors from nonphotosynthetic eubacteria, *Science* 286 (1999) 2517–2520.
- [10] L. Wu, R.S. McGrane, G.A. Beattie, Light regulation of swarming motility in *Pseudomonas syringae* integrates signaling pathways mediated by a bacteriophytochrome and a LOV protein, *MBio* 4 (2013) (e00334–13).
- [11] A. Bateman, L. Coin, R. Durbin, R.D. Finn, V. Hollich, S. Griffiths-Jones, et al., The Pfam protein families database, *Nucleic Acids Res.* 32 (2004) D138–D141.
- [12] A. Moglich, R.A. Ayers, K. Moffat, Structure and signaling mechanism of Per–ARNT–Sim domains, *Structure* 17 (2009) 1282–1294.
- [13] T.R. Berkelman, J.C. Lagarias, Visualization of bilin-linked peptides and proteins in polyacrylamide gels, *Anal. Biochem.* 156 (1986) 194–201.
- [14] S. Klinke, L.H. Otero, J. Rinaldi, S. Sosa, B.G. Guimaraes, W.E. Shepard, et al., Crystallization and preliminary X-ray characterization of the full-length bacteriophytochrome from the plant pathogen *Xanthomonas campestris* pv. *Campestris*, *Acta Crystallogr. F Struct. Biol. Commun.* 70 (2014) 1636–1639.
- [15] H. Takala, A. Bjorling, M. Linna, S. Westenhoff, J.A. Ihalainen, Light-induced changes in the dimerization interface of bacteriophytochromes, *J. Biol. Chem.* 290 (2015) 16383–16392.

- [16] F. Velazquez Escobar, P. Piwowarski, J. Salewski, N. Michael, M. Fernandez Lopez, A. Rupp, et al., A protonation-coupled feedback mechanism controls the signalling process in bathy phytochromes, *Nat. Chem.* 7 (2015) 423–430.
- [17] J.R. Wagner, J.S. Brunzelle, K.T. Forest, R.D. Vierstra, A light-sensing knot revealed by the structure of the chromophore-binding domain of phytochrome, *Nature* 438 (2005) 325–331.
- [18] L.O. Essen, J. Mailliet, J. Hughes, The structure of a complete phytochrome sensory module in the Pr ground state, *Proc. Natl. Acad. Sci. U.S.A.* 105 (2008) 14709–14714.
- [19] A.T. Ulijasz, R.D. Vierstra, Phytochrome structure and photochemistry: recent advances toward a complete molecular picture, *Curr. Opin. Plant Biol.* 14 (2011) 498–506.
- [20] K. Anders, G. Daminelli-Widany, M.A. Mroginski, D. von Stetten, L.O. Essen, Structure of the cyanobacterial phytochrome 2 photosensor implies a tryptophan switch for phytochrome signaling, *J. Biol. Chem.* 288 (2013) 35714–35725.
- [21] J.R. Wagner, J. Zhang, D. von Stetten, M. Gunther, D.H. Murgida, M.A. Mroginski, et al., Mutational analysis of *Deinococcus radiodurans* bacteriophytochrome reveals key amino acids necessary for the photochromicity and proton exchange cycle of phytochromes, *J. Biol. Chem.* 283 (2008) 12212–12226.
- [22] D. von Stetten, S. Seibeck, N. Michael, P. Scheerer, M.A. Mroginski, D.H. Murgida, et al., Highly conserved residues Asp-197 and His-250 in Agp1 phytochrome control the proton affinity of the chromophore and Pfr formation, *J. Biol. Chem.* 282 (2007) 2116–2123.
- [23] X. Yang, Z. Ren, J. Kuk, K. Moffat, Temperature-scan cryocrystallography reveals reaction intermediates in bacteriophytochrome, *Nature* 479 (2011) 428–432.
- [24] H. Takala, A. Bjorling, O. Bernthsson, H. Lehtivuori, S. Niebling, M. Hoernke, et al., Signal amplification and transduction in phytochrome photosensors, *Nature* 509 (2014) 245–248.
- [25] D. Bellini, M.Z. Papiz, Structure of a bacteriophytochrome and light-stimulated protomer swapping with a gene repressor, *Structure* 20 (2012) 1436–1446.
- [26] X. Yang, J. Kuk, K. Moffat, Crystal structure of *Pseudomonas aeruginosa* bacteriophytochrome: photoconversion and signal transduction, *Proc. Natl. Acad. Sci. U.S.A.* 105 (2008) 14715–14720.
- [27] M.A. Mroginski, D. von Stetten, F.V. Escobar, H.M. Strauss, S. Kaminski, P. Scheerer, et al., Chromophore structure of cyanobacterial phytochrome Cph1 in the Pr state: reconciling structural and spectroscopic data by QM/MM calculations, *Biophys. J.* 96 (2009) 4153–4163.
- [28] D. von Stetten, M. Gunther, P. Scheerer, D.H. Murgida, M.A. Mroginski, N. Krauss, et al., Chromophore heterogeneity and photoconversion in phytochrome crystals and solution studied by resonance Raman spectroscopy, *Angew. Chem. Int. Ed. Eng.* 47 (2008) 4753–4755.
- [29] J. Salewski, F.V. Escobar, S. Kaminski, D. von Stetten, A. Keidel, Y. Rippers, et al., Structure of the biliverdin cofactor in the Pfr state of bathy and prototypical phytochromes, *J. Biol. Chem.* 288 (2013) 16800–16814.
- [30] E. Krissinel, K. Henrick, Inference of macromolecular assemblies from crystalline state, *J. Mol. Biol.* 372 (2007) 774–797.
- [31] H. Li, J. Zhang, R.D. Vierstra, Quaternary organization of a phytochrome dimer as revealed by cryoelectron microscopy, *Proc. Natl. Acad. Sci. U.S.A.* 107 (2010) 10872–10877.
- [32] E.S. Burgie, T. Wang, A.N. Bussell, J.M. Walker, H. Li, R.D. Vierstra, Crystallographic and electron microscopic analyses of a bacterial phytochrome reveal local and global rearrangements during photoconversion, *J. Biol. Chem.* 289 (2014) 24573–24587.
- [33] H. Takala, A. Bjorling, M. Linna, S. Westenhoff, J.A. Ihalainen, Light-induced changes in the dimerization interface of bacteriophytochromes, *J. Biol. Chem.* (2015).
- [34] A.M. Jones, H.P. Erickson, Domain structure of phytochrome from *Avena sativa* visualized by electron microscopy, *Photochem. Photobiol.* 49 (1989) 479–483.
- [35] X. Yang, J. Kuk, K. Moffat, Conformational differences between the Pfr and Pr states in *Pseudomonas aeruginosa* bacteriophytochrome, *Proc. Natl. Acad. Sci. U.S.A.* 106 (2009) 15639–15644.
- [36] E.A. Stojkovic, K.C. Toh, M.T. Alexandre, M. Baclayon, K. Moffat, J.T. Kennis, FTIR spectroscopy revealing light-dependent refolding of the conserved tongue region of bacteriophytochrome, *J. Phys. Chem. Lett.* 5 (2014) 2512–2515.
- [37] X. Yang, E.A. Stojkovic, W.B. Ozarowski, J. Kuk, E. Davydova, K. Moffat, Light signaling mechanism of two tandem bacteriophytochromes, *Structure* 23 (2015) 1179–1189.
- [38] E.S. Burgie, R.D. Vierstra, Phytochromes: an atomic perspective on photoactivation and signaling, *Plant Cell* 26 (2014) 4568–4583.
- [39] E.S. Burgie, A.N. Bussell, J.M. Walker, K. Dubiel, R.D. Vierstra, Crystal structure of the photosensing module from a red/far-red light-absorbing plant phytochrome, *Proc. Natl. Acad. Sci. U.S.A.* 111 (2014) 10179–10184.
- [40] V. Anantharaman, S. Balaji, L. Aravind, The signaling helix: a common functional theme in diverse signaling proteins, *Biol. Direct* 1 (2006) 25.
- [41] M. Hulko, F. Berndt, M. Gruber, J.U. Linder, V. Truffault, A. Schultz, et al., The HAMP domain structure implies helix rotation in transmembrane signaling, *Cell* 126 (2006) 929–940.
- [42] A. Moglich, R.A. Ayers, K. Moffat, Design and signaling mechanism of light-regulated histidine kinases, *J. Mol. Biol.* 385 (2009) 1433–1444.
- [43] M.P. Bhate, K.S. Molnar, M. Goulian, W.F. DeGrado, Signal transduction in histidine kinases: insights from new structures, *Structure* 23 (2015) 981–994.
- [44] A. Marina, C.D. Waldburger, W.A. Hendrickson, Structure of the entire cytoplasmic portion of a sensor histidine-kinase protein, *EMBO J.* 24 (2005) 4247–4259.
- [45] S. Yamada, H. Sugimoto, M. Kobayashi, A. Ohno, H. Nakamura, Y. Shiro, Structure of PAS-linked histidine kinase and the response regulator complex, *Structure* 17 (2009) 1333–1344.
- [46] P. Casino, V. Rubio, A. Marina, Structural insight into partner specificity and phosphoryl transfer in two-component signal transduction, *Cell* 139 (2009) 325–336.
- [47] D. Albanesi, M. Martin, F. Trajtenberg, M.C. Mansilla, A. Haouz, P.M. Alzari, et al., Structural plasticity and catalysis regulation of a thermosensor histidine kinase, *Proc. Natl. Acad. Sci. U.S.A.* 106 (2009) 16185–16190.
- [48] R.P. Diensthuber, M. Bommer, T. Gleichmann, A. Moglich, Full-length structure of a sensor histidine kinase pinpoints coaxial coiled coils as signal transducers and modulators, *Structure* 21 (2013) 1127–1136.
- [49] M.H. Ryu, I.H. Kang, M.D. Nelson, T.M. Jensen, A.I. Lyuksyutova, J. Siltberg-Liberles, et al., Engineering

- adenylate cyclases regulated by near-infrared window light, *Proc. Natl. Acad. Sci. U.S.A.* 111 (2014) 10167–10172.
- [50] D.M. Shcherbakova, A.A. Shemetov, A.A. Kaberniuk, V.V. Verkhusha, Natural photoreceptors as a source of fluorescent proteins, biosensors, and optogenetic tools, *Annu. Rev. Biochem.* 84 (2015) 519–550.
- [51] Y.I. Wu, D. Frey, O.I. Lungu, A. Jaehrig, I. Schlichting, B. Kuhlman, et al., A genetically encoded photoactivatable Rac controls the motility of living cells, *Nature* 461 (2009) 104–108.
- [52] J. Gasteiger, Chemoinformatics: a new field with a long tradition, *Anal. Bioanal. Chem.* 384 (2006) 57–64.
- [53] W. Kabsch, Xds, *Acta Crystallogr. D Biol. Crystallogr.* 66 (2010) 125–132.
- [54] M.D. Winn, C.C. Ballard, K.D. Cowtan, E.J. Dodson, P. Emsley, P.R. Evans, et al., Overview of the CCP4 suite and current developments, *Acta Crystallogr. D Biol. Crystallogr.* 67 (2011) 235–242.
- [55] B.W. Matthews, Solvent content of protein crystals, *J. Mol. Biol.* 33 (1968) 491–497.
- [56] A.J. McCoy, R.W. Grosse-Kunstleve, P.D. Adams, M.D. Winn, L.C. Storoni, R.J. Read, Phaser crystallographic software, *J. Appl. Crystallogr.* 40 (2007) 658–674.
- [57] P. Emsley, B. Lohkamp, W.G. Scott, K. Cowtan, Features and development of coot, *Acta Crystallogr. D Biol. Crystallogr.* 66 (2010) 486–501.
- [58] G. Bricogne, E. Blanc, M. Brandl, C. Flensburg, P. Keller, W. Paciorek, et al., BUSTER Version X.Y.Z. Global Phasing Ltd., Cambridge, United Kingdom, 2011.
- [59] V.B. Chen, W.B. Arendall 3rd, J.J. Headd, D.A. Keedy, R.M. Immormino, G.J. Kapral, et al., MolProbity: all-atom structure validation for macromolecular crystallography, *Acta Crystallogr. D Biol. Crystallogr.* 66 (2010) 12–21.
- [60] E. Krissinel, K. Henrick, Secondary-structure matching (SSM), a new tool for fast protein structure alignment in three dimensions, *Acta Crystallogr. D Biol. Crystallogr.* 60 (2004) 2256–2268.
- [61] R.A. Laskowski, M.B. Swindells, LigPlot+: multiple ligand–protein interaction diagrams for drug discovery, *J. Chem. Inf. Model.* 51 (2011) 2778–2786.
- [62] T.A. de Beer, K. Berka, J.M. Thornton, R.A. Laskowski, PDBsum additions, *Nucleic Acids Res.* 42 (2014) D292–D296.
- [63] F. Sievers, A. Wilm, D. Dineen, T.J. Gibson, K. Karplus, W. Li, et al., Fast, scalable generation of high-quality protein multiple sequence alignments using Clustal Omega, *Mol. Syst. Biol.* 7 (2011) 539.
- [64] R.D. Finn, A. Bateman, J. Clements, P. Coghill, R.Y. Eberhardt, S.R. Eddy, et al., Pfam: the protein families database, *Nucleic Acids Res.* 42 (2014) D222–D230.
- [65] L.L.C. Schrodinger, The PyMOL Molecular Graphics System, Version 1.3r1, 2010.
- [66] M.A. Mroginiski, F. Mark, W. Thiel, P. Hildebrandt, Quantum mechanics/molecular mechanics calculation of the Raman spectra of the phycocyanobilin chromophore in alpha-C-phycocyanin, *Biophys. J.* 93 (2007) 1885–1894.
- [67] B.R. Brooks, C.L. Brooks III, A.D. Mackerell Jr., L. Nilsson, R.J. Petrella, B. Roux, et al., CHARMM: the biomolecular simulation program, *J. Comput. Chem.* 30 (2009) 1545–1614.
- [68] J.C. Phillips, R. Braun, W. Wang, J. Gumbart, E. Tajkhorshid, E. Villa, et al., Scalable molecular dynamics with NAMD, *J. Comput. Chem.* 26 (2005) 1781–1802.
- [69] ChemShell, A computational chemistry shell, [www.chem-shell.org](http://www.chem-shell.org).
- [70] D. Bakowies, W. Thiel, Hybrid models for combined quantum mechanical and molecular mechanical approaches, *J. Phys. Chem.* 100 (1996) 10580–10594.
- [71] M.J. Frisch, G.W. Trucks, H.B. Schlegel, G.E. Scuseria, M.A. Robb, J.R. Cheeseman, et al., Gaussian 09, Gaussian, Inc., Wallingford, CT, USA, 2009.
- [72] G. Rauhut, P. Pulay, Transferable scaling factors for density functional derived vibrational force fields, *J. Phys. Chem.* 99 (1995) 3093–3100.
- [73] P.V. Afonine, N.W. Moriarty, M. Mustyakimov, O.V. Sobolev, T.C. Terwilliger, D. Turk, et al., FEM: feature-enhanced map, *Acta Crystallogr. D Biol. Crystallogr.* 71 (2015) 646–666.
- [74] R.A. Engh, R. Huber, “Accurate bond and angle parameters for X-ray protein structure refinement, *Acta Crystallogr. A* 47 (1991) 392–400.